Carbothermal reduction of phosphogypsum waste using coal

Luke Jordan
15123643

Department of Chemical Engineering
University of Pretoria
South Africa

2021-10-25

Carbothermal reduction of phosphogypsum waste using coal

Abstract

Phosphogypsum waste represents a potential source for the recovery of elemental sulphur, rare earth elements, and calcium carbonate. With primary interest on the reducing step of the process, converting the sulphates to sulphides, there is good precedence shown that the reduction of phosphogypsum can be realised carbothermally. Coal should serve as a suitable source of carbon for the process step, with the ready availability of coal and relatively low cost being key factors in its choice.

Calcium sulphate is reduced within a temperature range of 850–1100 °C, with an unfavourable side reaction, that produces calcium oxide, that can initiate at 900 °C depending on process conditions. The side reaction is an oxidative reaction, and its negative impact can thus be mitigated by charging sufficient excess carbon which serves to maintain the reducing conditions required for the primary reaction.

The reduction is generally believed to be facilitated by a gaseous intermediate acting as the reducing agent. The presence of O_2 and CO_2 are undesirable as they favour the production of calcium oxide and calcium sulphate rather than the sulphide. It is recommended that, for the use of coal as carbonaceous material, an inert environment (such as a nitrogen atmosphere) should be created to carry out the reduction.

The addition of catalysts such as ferric oxide or potassium dichromate can enhance the reaction satisfactorily and reduce the initiation temperature to approximately 750 °C and increase the yield of calcium sulphide.

Heat transfer within the reacting bed of phosphogypsum and coal is modelled by means of a two-dimensional transient finite difference method. The model's scope has been limited from describing the entire furnace and all the involved conductive, convective, and radiant heat transfer to rather focus on the heat transfer within the reacting material contained in the furnace.

The kinetics of the reaction is used to develop a relationship between the temperature of a node in the two-dimensional mesh and the correlating composition of said node. This change in composition is incorporated into the model by adjusting the heat transfer

properties (C_p, α, τ) used in the heat transfer calculation for each node respective to its temperature.

The model is validated against experimental data, captured using an array of thermocouples placed throughout the reacting mixture in a three-inch and six-inch crucible. The vessels were heated to 1000 °C with a heating rate of 3 °C min^{-1} while purging with nitrogen gas.

The model achieves conservative results, over-predicting the time required to reach 1000 °C. It can be noted that improvement in model accuracy can be achieved by varying the pre-exponential factor and the thermal conductivity of the system. However, the effect the thermal conductivity has is far more substantial than the rate of reaction for the system. This indicates that the thermal conductivity values available from literature (which are limited) do not describe the system with sufficient accuracy and as such, it would be beneficial to study the thermal conductivity. Application of a model that varies thermal conductivity linearly with temperature achieves reasonable results and matches the trends observed in experimental results well. However, it is still recommended that larger scale experiments be conducted as the model shows increasing inaccuracy as the mass and vessel diameter increase.

A sensitivity analysis for a hypothetical tunnel kiln is used to determine the optimum cylindrical vessel configuration to maximise the possible material processing rate. The analysis found that a shallower material bed results in a more optimal setup, with more efficient heat transfer. This results in an estimated processing rate 771 Mt per year, which is not unrealistic based on similar tunnel kilns used in the direct reduction of iron. However, the design of a furnace is a complicated process with many variables, so these results are far from conclusive and it is recommended to determine whether a shallow square/cubic configuration is better suited.

The model has good flexibility and can be updated and improved readily. Conservative results indicate a good applicability for the model in industrial scenarios where factors of safety are necessary. The model shows good suitability for the prediction of the heat transfer occurring within a reacting bed of solid phosphogypsum and coal.

Contents

Nomenclature

Abbreviations

AMD Acid mine drainage

GCC Ground calcium carbonate

PCC Precipitated calcium carbonate

REE Rare earth element

Mathematical Symbols

α Thermal diffusivity ($m^2\ s^{-1}$)

$\dot{Q}$ Heat flow (W)

$\dot{q}$ Heat generated in a medium ($W\ m^{-3}$)

ρ Density ($kg\ m^{-3}$)

τ Mesh Fourier number (-)

C_p Heat capacity ($J\ kg^{-1}\ K^{-1}$)

E Energy (J)

fr_i Mass / volume fraction of component i (-)

k Thermal conductivity ($W\ m^{-1}\ K^{-1}$)

k_i Arrhenius rate constant (s^{-1})

$k_{i(0)}$ Arrhenius pre-exponential factor (s^{-1})

l Length (m)

R Ideal gas constant ($J\ mol^{-1}\ K^{-1}$)

r Radial distance (m)

T Temperature (K)

t Time (s)

V Volume (m^3)

z Vertical distance (m)

1 Introduction

Millions of tons of phosphogypsum- and gypsum-rich solid wastes and sludge are generated by the chemical manufacturing industry and the industrial waste remediation sector. Gypsum is a by-product of many processes, including the production of phosphoric, hydrofluoric, citric and boric acids, treatment of waste from desulphurisation of flue gases from coal-fired power stations, ore smelting and acid mine water treatment. Phosphogypsum is, in contrast, primarily formed as a by-product of the production of fertiliser from phosphate rock. Although gypsum is widely used in the construction industry, phosphogypsum is generally regarded as unsuitable for further use, and is stored indefinitely in large stockpiles. These stacks are becoming substantial expenses for the industry, occupying significant areas of land and being subject to the tightening of regulations on waste materials and their disposal. As an example of further complications that can arise from the disposal of gypsum, the remediation of acid mine drainage (AMD) using alkaline-based processes gives rise to a gypsum-rich sludge which requires proper environmental management in order to prevent serious environmental pollution such as airborne dust and contamination of groundwater resources (Macías, Caraballo & Nieto, 2012).

Costs associated with the transportation and storage of phosphogypsum in dumps can be high at about 18 % of the cost of phosphoric acid production, with a significant increase during the transition to more reliable hydrotransport for the phosphogypsum. Operating costs are estimated at 12 % of the cost of raw material processing (Yunusova, 2004). Kozicki & Carlson (2020) estimate the cost to dispose of phosphogypsum at $125 per ton of P_2O_5, however notes that this figure does not include costs associated with long-term liability or incurred in the event of a catastrophe for environmental cleanup, nor does it account for the especially costly endeavour of permanently closing a stack at the end of its useful life.

Similarly, about one-third of the global production of sodium sulphate (Na_2SO_4) is as a waste or byproduct in other industrial processes, such as rayon manufacture, precipitated silica production, flue gas desulphurisation, spent battery processing, neutralisation and the regeneration of ion-exchange resins. The salt concentrations in such streams can vary substantially. With regards to disposal, diluted waste salt solutions are simply sewered as their purification is considered non-economic given the high cost and energy consumption. There is a considerable investment and operational cost involved with purification and treatment of more concentrated solutions (Nowak, Jaroszek & Turkowska, 2014).

An alternative approach to the often expensive management of stockpiles is to treat the waste with the aim of converting it into potentially useful products (de Beer *et al*, 2014; Tao *et al*, 2001).

Phosphogypsum and sodium sulphate waste can represent a good resource for the recovery of elemental sulphur (S) —$106 per ton (WTO, 2018a), calcium carbonate ($CaCO_3$) — $114 per ton (WTO, 2018b), and sodium carbonate (Na_2CO_3) —$190 per ton (WTO, 2018c), respectively. Gypsum generated during the production of phosphoric acid, also known as phosphogypsum, contains rare earth elements (REEs) and could constitute a potential secondary source of the metals (Kulczycka *et al*, 2016; Walawalkar, Nichol & Azimi, 2016).

Sulphur is a key raw material for many manufacturing industries including the production of acids, explosives, fertilisers, insecticides, steel and titanium dioxide (Cork, Jerger & Maka, 1986). Cork *et al* (1986) also suggests sulphur's application as an alternative feedstock for the production of polymeric materials. Calcium carbonate sees use in a wide variety of commercial applications in one of two main forms, ground calcium carbonate (GCC) and precipitated calcium carbonate (PCC). GCC features in the manufacture of concrete or Portland cement, lime to be used in soil stabilisation and acid neutralisation, and can be used for water treatment and flue gas desulphurisation (Oates, 1986). PCC sees extensive use as a filler and coating pigment in paper, plastics, paints, rubbers and adhesives (Windholz, 1983; Zhang *et al*, 2010). Sodium carbonate also serves a number of different industries, such as: the manufacture of glass, where it is used as a flux for silica; as a water softening agent, to remove Mg^{2+} and Ca^{2+} ions; a food additive, used as an acidity regulator, anti-caking agent, raising agent, and stabiliser. Other uses include the manufacture of paper, rayon, soaps and detergents (Thieme, 2000).

REEs see widespread use due to their physical and chemical properties, which include magnetism, luminescence, conductivity, electro-optical and nuclear properties (Akah, 2017). Rare earths have contributed to the improvement of the operating efficiency, longevity, miniaturisation of components and to the complexity and footprint of many industrial, military and space instruments. REE use is further growing as the development of new applications and expansion of current rare earth consumer industries continues (Dutta *et al*, 2016).

However, the process to recover these materials (sulphur, calcium- and sodium carbonate) entails *inter alia* carbothermal reduction of the sulphate salts in the waste products to form sulphide salts that can then be converted into forms that are saleable. Additionally, although REEs can be recovered directly, the reduction serves to concentrate the rare earths before their extraction.

It has been concluded that a continuously operated tunnel kiln might be the best type of kiln to use for the carbothermal reduction step, but suitable design information is currently not available to design and construct such a kiln with confidence.

In the envisaged continuous tunnel kiln the solid waste will pass through three distinctive zones, a pre-heating, a reduction and a cooling zone. The off-gas from the reduction of the solids, containing carbon monoxide and hydrogen, will be used as the source of energy for the endothermic reduction process by combusting it outside the above-mentioned reduction zone and transferring heat indirectly into the reduction zone. Furthermore the off-gas from the combustion will flow via heat exchange tubes counter-currently to the solid feed through the pre-heating zone. In order to enhance the heat transfer from the hot combustion gases to the solids being processed, high temperature fans will be installed to circulate gas inside the pre-heating section of the kiln.

Building, operating and maintaining such a continuous tunnel kiln pilot plant is deemed to be too expensive and too risky with respect to the current stage of technology maturity, it is therefore proposed to gain critical design and operating information by testing a batch kiln that can replicate slices out of a continuous kiln at various positions along the travel of the feed through the kiln.

A batch operated kiln, capable of loading 10–15 kg samples, will be built such that it can be heated indirectly using similar means as a continuous kiln to transfer heat from an energy source. By programming the temperature profile and adjusting the flow of circulating gases through the kiln, the various zones in the continuous kiln can be replicated, the heat transfer rates measured, the overall reduction process simulated and the integrity of the required equipment and materials of construction verified.

2 Theory

2.1 Calcium sulphate waste

Nengovhela *et al* (2007) proposed a multi-step process for the recovery of sulphur and $CaCO_3$ from gypsum waste. It involves the following three steps:

1. Thermal reduction (850–1100 °C) of gypsum waste to produce calcium sulphide (CaS) using a reducing agent (*eg* solid carbon materials such as coal or activated carbon (Equation 1), carbon monoxide gas (Equation 2), or hydrogen gas (Equation 3))

$$CaSO_4(s) + 2C(s) \longrightarrow CaS(s) + 2CO_2(g) \quad (1)$$

$$CaSO_4(s) + 4CO(g) \longrightarrow CaS(s) + 4CO_2(g) \quad (2)$$

$$CaSO_4(s) + 4H_2(g) \longrightarrow CaS(s) + 4H_2O(g) \quad (3)$$

2. Direct aqueous carbonation of CaS to produce hydrogen sulphide (H_2S) and $CaCO_3$:

$$CaS(s) + H_2O(l) + CO_2(g) \longrightarrow H_2S(g) + CaCO_3(s) \tag{4}$$

3. Production of sulphur from H_2S via the commercially available Clauss process (Mark *et al*, 1978), which follows

$$2H_2S + 3O_2 \longrightarrow 2SO_2 + 2H_2O \tag{5}$$
$$4H_2S + 2SO_2 \longrightarrow 3S_2 + 4H_2O \tag{6}$$

Understanding of process steps 1 and 3 has been developed quite well by numerous authors (Kato, Murakami & Sugawara, 2012; Ma *et al*, 2011; Miao *et al*, 2012; Ning *et al*, 2011; Ruto *et al*, 2011; Selim, Gupta & Al Shoaibi, 2013; Sliger, 1988; Zhang *et al*, 2010). Contributions to the the understanding of step 2 include two independent studies by Nengovhela *et al* (2007) on the stripping of H_2S, and by Brooks & Lynn (1997) on the conversion of CaS into H_2S and $CaCO_3$ by making use of methyldiethanolamine as a complexing agent for CO_2 and H_2S. De Beer *et al* (2014) studied process step 2 to better understanding of the direct aqueous carbonation by investigating both the solution chemistry of the process & the properties of the formed product.

Sliger (1988) and de Beer *et al* (2015) proposed an alternative to step two, whereby an indirect aqueous carbonation process can be used to produce high-grade $CaCO_3$ ($\geq$ 99 wt %, as opposed to the $\leq$ 90 % from step 2) or precipitated calcium carbonate. The process by de Beer *et al* (2015) is still under development and optimisation, but Sliger (1988) proposes the Kel-S process which is based on the concept of reducing the sulphates to sulphide, converting to water soluble hydrosulphide, separating the dissolved hydrosulphide from insoluble impurities and finally producing ultra-pure calcium carbonate and gaseous hydrogen sulphide by means of carbonation.

With regards to the batch furnace to be designed, process step 1 is the step of interest as it describes the desired reaction. The product in question, calcium sulphide (CaS) which melts at 2525 °C, is a hygroscopic white crystal that hydrolyses in water. It occurs as oldhamite in nature. CaS has an odor of rotten eggs, which stems from H_2S formed by hydrolysis of the calcium sulphide (Ullmann, 2008).

The reduction of the sulphate is fairly straightforward, but not without complications. A secondary reaction, given by

$$3CaSO_4 + CaS \rightarrow 4CaO + 4SO_2 \tag{7}$$

can also occur (initiating at 900 °C), however, as this is an oxidative reaction with respect to CaS, sufficient excess carbonaceous material serves to mitigate the reaction's impact (Mbhele *et al*, 2009; Strydom, Groenewald & Potgieter, 1997).

Typically the choice of kiln to perform the reduction to CaS in is a rotary kiln, using charcoal and phosphogypsum as the sources of carbon and the sulphate respectively.

Charcoal is not the only reducing agent that can be used however: coal, coke, methane, carbon monoxide, and hydrogen can also be used to reduce calcium sulphate to calcium sulphide, but, as mentioned, temperatures over 850 °C are required to obtain near-stoichiometric conversions (Li & Zhuang, 1999).

It was found when using coal that the pelletisation of gypsum-coal mixtures resulted in higher sulphide yields when compared to non-pelletised mixtures (Nengovhela *et al*, 2007). In a further pelletisation investigation performed by Motaung *et al* (2015), two binders were tested, starch and microcrystalline cellulose, and were found to have slight catalytic effects on the reduction while acting as satisfactory binders.

Considering catalytic effects, Strydom *et al* (1997) showed that the addition of 5 wt % of ferric oxide (Fe_2O_3) can reduce the initiation temperature to approximately 750 °C. Furthermore, Kale, Pande & Gokarn (1992) studied the effect of various catalysts impregnated in the matrix of carbon and discovered that mixed catalysts such as potassium dichromate can enhance the reaction rate quite satisfactorily and the reaction can take place at 740–860 °C. It was also discovered that some additives, especially a semicoke of coal that contains > 20 % volatiles in dry matter in a mixture with ferric oxide can intensify the calcium sulphide recovery process and raise the calcium sulphide yield (Trikkel & Kuusik, 1994). Whereas, Zadick, Zavaleta & McCandless (1972) found that ferric oxide, stannous sulphate and vanadium pentoxide have pronounced catalytic effect on the reduction of calcium sulphate.

Several authors have reported that the main reducing agent during the thermal reduction process to be the gaseous intermediate (Gorkan *et al*, 2000; Oh & Wheelock, 1990). To this end, it has also been found that the presence of O_2 and CO_2 are undesirable as they favour the formation calcium oxide and calcium sulphate. Thus, as reported by Jagtap, Pande & Gokarn (1990), to effectively favour the formation of CaS from $CaSO_4$ an excess of carbon monoxide (if using a gaseous reducing agent) in the kiln should be present, alternatively, if a solid reducing agent is being used, an environment that favours excess amounts of CO in the kiln is desirable (Motaung *et al*, 2015).

As reported by Yan *et al* (2014), and corroborated by Mbhele *et al* (2009) and Motaung *et al* (2015), temperature plays an important role in the conversion of the sulphate, where

the increased yield with increasing temperature can be seen in Figure 1.

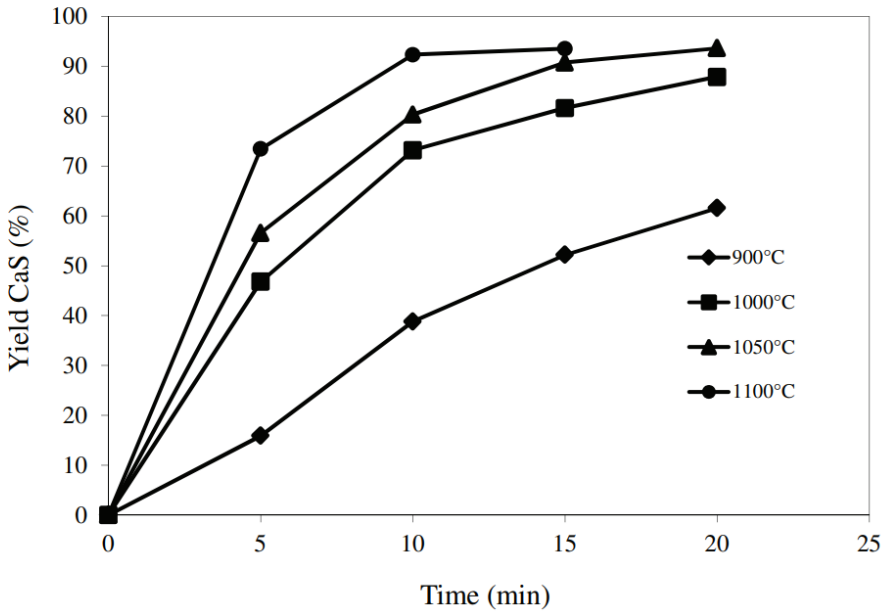

Figure 1: Conversion curves of thermo-reduction studies of waste gypsum sludge from AMD neutralization (Motaung *et al*, 2015)

The study performed by Mbhele *et al* (2009), which focused on the recovery of sulphur from waste gypsum using activated carbon, investigated several process conditions to determine their impact on the yield of CaS and subsequently sulphur. Naturally, a longer reaction time yielded greater conversions, with sufficient residence time being noted at 20 min for a sample of approximately 180 g. It was also found that CaO production (as per Equation 7) was favoured at low carbon to gypsum ratios, and CaS becomes favoured at carbon to gypsum ratios greater than 2, with higher yields as carbon content increases. Furthermore, it was found that as the average particle size of the mixture decreases, improved conversions can be achieved. Lastly, Mbhele *et al* (2009) estimated that from 1 ton of pure gypsum, 0.18 ton of sulphur and 0.58 ton of $CaCO_3$ could be recovered.

2.1.1 Rare earth elements

The extraction of these REEs is beyond the scope of the carbothermal reduction to be presented, but forms an integral part of the economic feasibility of the process as a whole, and as such, it is noteworthy, albeit anecdotally.

During phosphoric acid production, 70–85 % of the REEs from the phosphate rocks (estimated to be 0.8–1 wt %, depending on the source and type of rock) used in the process are said to be found in the phosphogypsum due to the incorporation of REEs in the sulphate's crystal lattice during precipitation (Kulczycka *et al*, 2016; Peelman *et al*, 2016; Walawalkar *et al*, 2016). Due to the high volume of phosphogypsum produced and its chemical stability, the rare earths are considered to be lost (Peelman *et al*, 2016).

There have been numerous studies into the recovery of these rare earths from phosphogypsum and consequently varying suggested techniques (Kulczycka *et al*, 2016). These techniques include: leaching using sulphuric acid followed by either evaporation or neutralisation; precipitation using hydrofluoric acid; extraction with nonyl-phenyl phosphoric acid. Pyro-, hydro- and electromechanical processes also feature amongst the common techniques used, but in the case of phosphogypsum, hydrometallurgical processes tend to be the preferred choice (Tunsu *et al*, 2015; Walawalkar *et al*, 2016).

The carbothermal reduction facilitates further concentration of these rare earths from the phosphogypsum from ±0.4 % in the phosphogypsum to ±4 % in the residue after sulphur and calcium carbonate recovery. However, the extraction is a field of research and development in its own right.

2.2 Sodium sulphate waste

Similar to calcium sulphate, sodium sulphate is carbothermaly reduced to produce sodium sulphide, with an initiation temperature ranging from 700–900 °C depending on the reducing agent used and presence of catalysts. Sodium sulphide is a crystalline chemical with the formula Na_2S, and a melting point of 1170 °C. It exists more commonly as its hydrate, $Na_2S{\cdot}9H_2O$. Sodium sulphide is readily soluble in water and is also appreciably soluble in lower alcohols, such as methanol or ethanol (Ullmann, 2008).

The reduction is not novel and the use of coal as a reducing agent has been in practice for decades (Ullmann, 2008). The reduction can also be performed with hydrogen, methane or other hydrocarbons, however focus shall be given to those processes that utilise coal as the reducing agent.

The reaction initiates within the temperature range of 700 to 900 °C in accordance to the following equation

$$Na_2SO_4 + 2C \rightarrow Na_2S + 2CO_2 \tag{8}$$

The temperature of initiation depends strongly on the reducing agent used and the presence of any catalysts. At approximately 745 °C, the evolution of Na_2S and CO_2 begins and the reaction mass becomes fluid as the reduction proceeds. Further reduction leads the reaction mass to become pasty and finally solid. This behaviour is due to a eutectic formed between sodium sulphate and sodium sulphide, as can be seen in Figure 2.

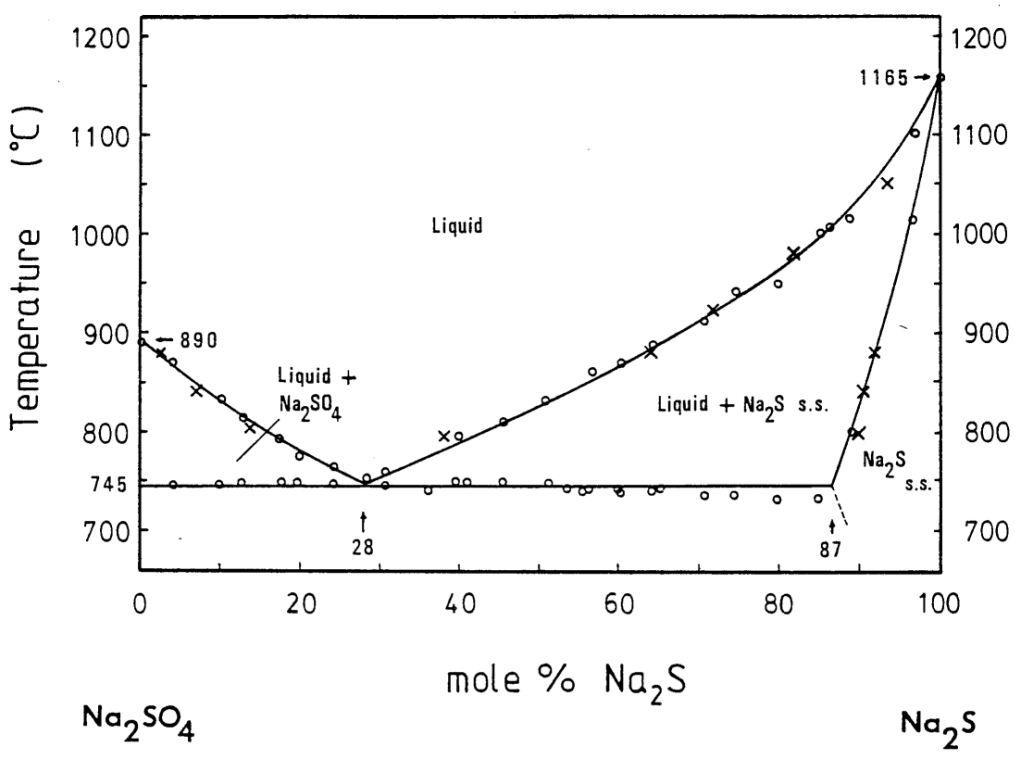

Figure 2: Sodium sulphate and sulphide phase diagram (Tran & Barham, 1981)

Commonly, the reaction is performed in either a reverberating or rotating-hearth furnace, with typical operating temperatures reaching 1100 °C. The lining of these furnaces are, however, strongly attacked by the sodium sulphide.

Na_2S produced in this fashion contains excess carbon, ash components, Na_2CO_3, $Na_2S_2O_3$, and Na_2SO_3. The reactor product is leached with water and undissolved compounds are filtered out. By evaporating the extraction liquor, either crystals of the composition $Na_2S{\cdot}9H_2O$ are obtained or, with further evaporation, a product containing 60–62 wt % Na_2S solidifies from the melt. These products contain considerable amounts of soda, sulphite, thiosulphate, sulphate and iron salts.

As an alternative in the post-processing treatment, the leaching of the reactor product can be performed with a solution of methanol to dissolve the sulphide, instead of using water. The product obtained by subjecting the extractant to evaporation is free of water, iron, sulphite, sulphate and thiosulphate.

Considering the reduction with carbon, there are a number of disadvantages to its use: at the reaction temperature liquefaction occurs; the carbon must be completely oxidised or the product is badly coloured and must be recrystallised; and it is typically a batch process (Nyman & O'Brien, 1947).

Budnikoff & Shilov (1971) conducted one of the earliest studies into the reduction of sodium sulphate, using carbon monoxide, hydrogen and carbon as reducing agents. They made use of an electric furnace, heating a platinum boat containing sodium sulphate while purging the system with inert or reducing gases.

The study showed that at 850 °C or below, carbon would not reduce sulphate under an inert atmosphere, however, when carbon monoxide or dioxide was used as purge gas the sulphate was reduced with yields of 80 % sulphide in less than an hour at 850 °C. With carbon as the reducing agent, the rate of reduction is strongly dependent on the nature of carbon. It was determined by White & White (1936) that coal and charcoal had the greatest reactivity, followed by lampblack and Acheson graphite respectively.

When considering gaseous reducing agents, Nyman & O'Brien (1947) determined that H_2 was the most effective, followed by H_2S, NH_3 and CH_4 respectively. These findings served in addition to the trend reported by Budnikoff & Shilov (1971) that the reactivity of H_2 was much greater than that of CO.

The liquefaction of the reaction components is a point of much contention. Although it is agreed the liquefaction is due to the formation of an eutectic between the sulphate and sulphide, there is no clear consensus on the composition of the eutectic. White & White (1936) noted, during melt tests varying the ratio of Na_2S to Na_2SO_4, that at 700 °C mixtures containing 34.6 and 42.5 % sulphide exhibited fusion and at 740 °C, all compositions between 15.0 and 68.9 % sulphide had shown a liquid phase. This is contrasted by a personal communication by Peck, conveyed by White & White (1936), that a eutectic is indicated at compositions of 25.1 and 30.0 % when examined petrographically. Nyman & O'Brien (1947) report mixtures of 30 and 50 % sulphide forming eutectics and melting at above 700 °C. Furthermore, Ley (1934) and Courtois (1939) report eutectics at 620 °C of 20 % sulphide and at 730 °C of 50 % sulphide respectively.

In terms of catalysts, several authors have reported that certain metals will catalyse the reduction, these findings have been summarised below in Table 1

Table 1: Summary of catalysts per reducing agent

Reducing agent	Catalyst
Hydrogen	Iron (oxide or sulphate) [1] Copper (II) sulphate [1] Carbon [2]
Carbon Monoxide	Carbon [3]
Coal	Lime [4]

[1] Nyman & O'Brien (1947)
[2] Birk *et al* (1971)
[3] Budnikoff & Shilov (1971)
[4] White & White (1936)

The use of catalysts is typically achieved by mixing the catalyst with starting material before pelletisation.

The reduction has been found to be autocatalytic for both solid and gaseous reducing agents, as indicated by Birk *et al* (1971) and Budnikoff & Shilov (1971).

White & White (1936) also performed extensive materials of construction tests for the sulphide system, testing nickel, porcelain, Chromel A, alundum, aluminum, quartz, monel metal, tungsten, tantalum, graphite and molybdenum. All of the materials were attacked to a considerable extent by the sodium sulphide, with the exception of graphite, however graphite does react with sodium sulphate making it unsuitable.

3 Furnace design

The batch kiln in mind is to be designed as a coffin-lid furnace, as opposed to a more typical muffle furnace. The advantages afforded by rather making use of a coffin-lid furnace include the prevention of gas leakages due to natural convection, caused by the density differences between the atmosphere inside and outside the kiln, that would occur through a muffle furnace's door seal. Furthermore, a coffin-lid furnace allows for better access to the kiln internals for maintenance or modification purposes.

3.1 Furnace materials

Two different refractory materials, sourced from Morgan Advanced Materials, have been selected for use in the design of the furnace. The roof of the furnace is to use pyro-log brick refractories, given their low density, while a firebrick refractory will be used in the rest of the furnace. Table 2 describes the properties of the selected refractory materials.

Table 2: Refractory materials properties (Morgan Advanced Materials, 2019)

Item	Value		Units
	Firebrick	Pyro-log	
Density	800	192	kg m^{-3}
Heat capacity	1100	1300	J kg^{-1} K^{-1}
Thermal conductivity at:			
400 °C	0.25	0.1	
600 °C	0.27	0.16	
800 °C	0.3	0.23	W m^{-1} K^{-1}
1000 °C	0.33	0.32	
1200 °C	0.35	-	

Subsequently, for use in model calculations, the firebrick and pyro-log materials' thermal conductivities are fitted using least squares regression to a linear and quadratic function as represented by Equations 9 and 10 for the firebrick and pyro-log respectively.

$$k = (1.3 \times 10^{-4})T + 0.1605 \quad (9)$$

$$k = (1.875 \times 10^{-7})T^2 + (6.875 \times 10^{-8})T + 0.0155 \quad (10)$$

The properties of 310 stainless steel, used for making the furnace crucibles are given in Table 3

Table 3: 310 stainless steel properties (Azo Materials, 2019)

Item	Value
Density	7940 kg m^{-3}
Heat capacity	510 J kg^{-1} K^{-1}
Thermal conductivity	13.5 W m^{-1} K^{-1}

While the silicon carbide based partitions, shown in Figure 3, are composed of 86, 11 and 3 mass % of silicon carbide (SiC), aluminium oxide (Al_2O_3), and calcium oxide (CaO) respectively. The density of the fired product is given as 2600 kg m^{-3} (Keramicalia,

2019). The heat capacity of the partition can be calculated using

$$C_{p_{\text{mixture}}} = \sum_{\text{components}} m_{fr} C_{p_i} \tag{11}$$

where the heat capacities of the components are calculated using the Shomate equation (Chase, 1998):

$$C_p = A + Bt + Ct^2 + Dt^3 + \frac{E}{t^2} \tag{12}$$

where $t = T/1000$ and the constants are given in Table 4 below

Table 4: Shomate constants for partition components (Chase, 1998)

Constant	Materials			
	SiC ($\leq$ 1000 K)	SiC ($>$ 1000 K)	Al_2O_3	CaO
A	20.55859	46.90222	102.429	49.95403
B	64.57962	5.845968	38.7498	4.887916
C	-52.98827	-1.08541	-15.9109	-0.352056
D	16.95813	0.093021	2.62818	0.46187
E	-0.781847	-3.448876	-3.007551	-0.825097

3.2 Thermal design

3.2.1 Preliminary sizing

The preliminary sizing of the batch kiln is based on the capacity to process 10–15 kg of feed.

With a molar feed ratio of fixed carbon to calcium sulphate of 2.5 to 1, and using the compositions as described by Tables 6 and 7 (Section 5), the mass feed ratio of coal to phosphogypsum can be calculated as 0.35 : 1. The bulk density of gypsum is given as 860 kg m^{-3} (Anval Valves, 2019; Binmaster, 2019), while that of bituminous coal is given as 673–913 kg m^{-3} (Engineering ToolBox, 2003a). However, a more conservative approach was used, as bulk density is a highly packing condition dependent value, the bulk densities were determined in-house to be 721.1 and 735 kg m^{-3} respectively, and bulk density of the mixture was determined as 836 kg m^{-3}. The volume of feed is approximately 12–17 L.

A cylindrical pot of 300 mm in diameter, with a wall thickness of 5 mm, was selected to serve as the base design case. The internal volume afforded for loading feedstock by such a vessel is 19.8 L, sufficient excess that exposure to risk of under-design is minimised.

Figure 3 depicts the chosen furnace design to accommodate this furnace pot, or multiple smaller pots, the fan, the heating elements and silicon carbide castable partitions.

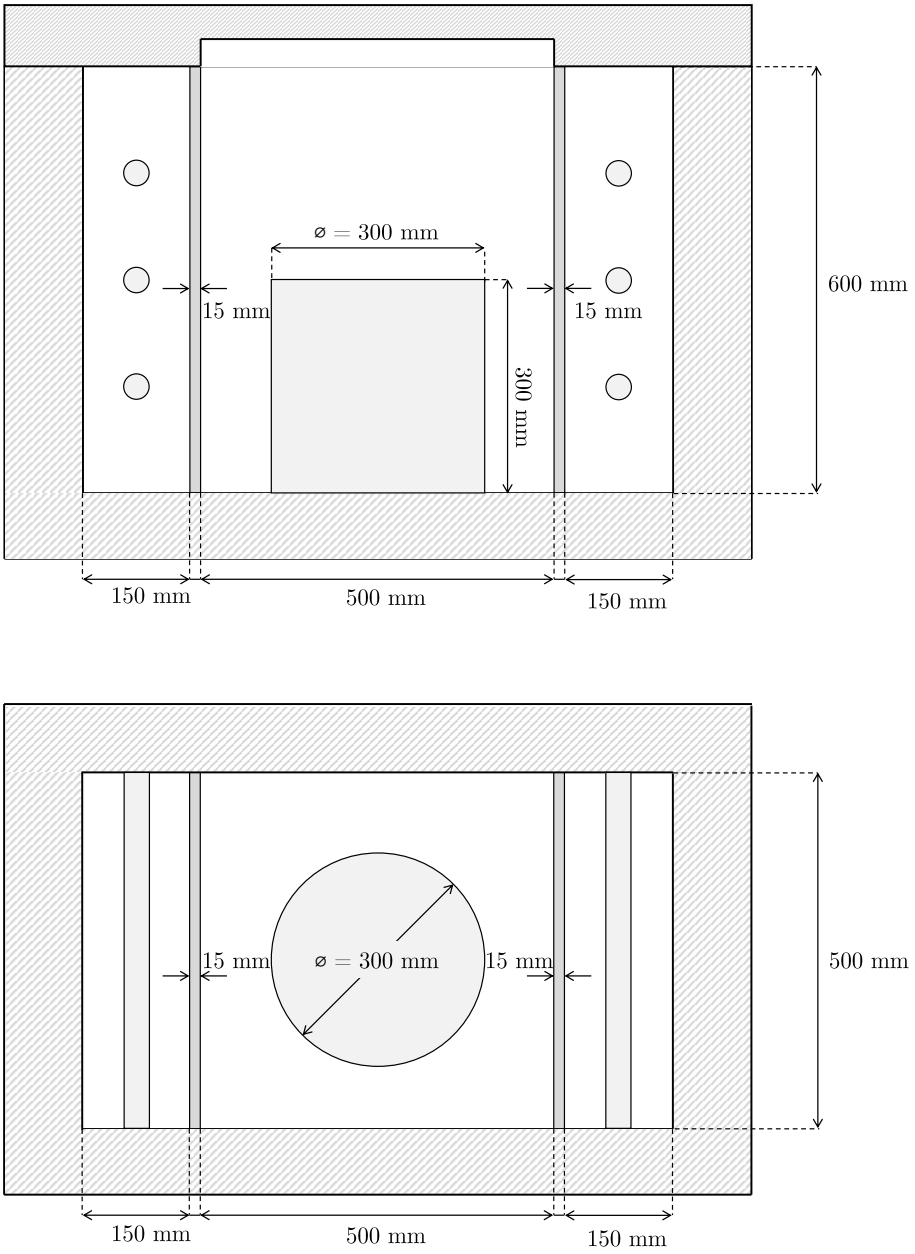

Figure 3: Preliminary furnace sketch

To determine the refractory wall thickness required, a steady state case was used to estimate a minimum thickness required. This value can then be corroborated using a transient model to simulate the walls' behaviour approaching and during steady state. This is discussed in Sections 3.2.2 and 3.2.3 respectively.

3.2.2 Steady state modelling

At steady state conditions, the only heat flow present is that of conduction through the wall, convective heat losses to the external environment surrounding the furnace and radiative heat losses. For the simplicity of calculation with the accuracy required, radiative heat losses were assumed to be negligible. Thus the conductive heat transfer, as described by Equation 13, through the wall is equal to that of the convective heat losses, as described by Equation 14.

$$Q = k(T)A\frac{\mathrm{d}T}{\mathrm{d}x} \tag{13}$$

$$Q = hA(T_s - T_\infty) \tag{14}$$

The steady state conditions are well described by Figure 4.

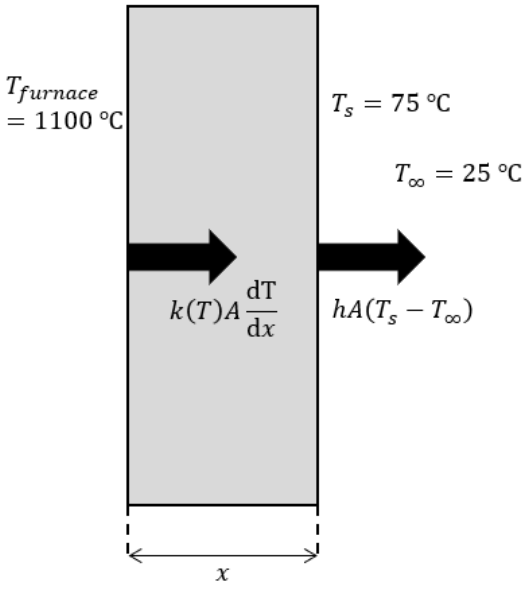

Figure 4: Steady state wall conditions

Using a convective heat transfer coefficient of 15 W m^{-1} K^{-1} (Çengel & Ghajar, 2015; Engineering ToolBox, 2003b), the wall thickness can be calculated for the firebrick and pyro-log based refractory walls as 380 mm and 220 mm respectively.

3.2.3 Transient modelling

To simplify the modelling procedure, a finite difference approach has been adopted, where a number of simplifying assumptions have been made, as follows:

1. The ramping rate is chosen such that in four hours the furnace temperature is at 1100 °C (≈ 4.5 °C min^{-1}).
2. The internal wall surface temperature is assumed to be equal to the temperature of the furnace. That is, an infinite convective heat transfer coefficient is assumed such that the internal surface temperature changes according to the ramping rate selected.
3. The external heat transfer coefficient remains constant.
4. Heat transfer only occurs in one dimension (laterally through the wall).
5. Radiative heat losses are assumed to be negligible.
6. Internal heat generation is neglected.

The formulation of the transient model, as described by Çengel & Ghajar (2015) and Welty, Wicks & Wilson (1969), begins with the energy balance on a volume element during a time interval, Δt, and can be expressed as

$$\Delta t \times \sum_{\text{All sides}} \dot{Q} + \Delta t \times \dot{q}_{\text{element}} = \Delta E_{\text{element}} \tag{15}$$

where the rate of heat transfer, $\dot{Q}$, consists of conduction terms for the interior nodes and involves both conduction and convection for the boundary node. Noting that $\Delta E_{\text{element}} = \rho V_{\text{element}} C_p \Delta T$, dividing Equation 15 by Δt for any node m in the medium and its volume element gives

$$\sum_{\text{All sides}} \dot{Q} + \dot{q}_{\text{element}} = \rho V_{\text{element}} C_p \frac{T_m^{i+1} - T_m^i}{\Delta t} \tag{16}$$

Excluding heat generation, the discretisation follows that, for an internal node, the explicit formulation can be expressed as

$$T_m^{i+1} = \tau(T_{m-1}^i + T_{m+1}^i) + (1 - 2\tau)T_m^i \tag{17}$$

and that of a boundary node

$$T_m^{i+1} = (1 - 2\tau - 2\tau\frac{h\Delta x}{k})T_m^i + 2\tau T_{m-1}^i + 2\tau\frac{h\Delta x}{k}T_{air} \tag{18}$$

where the symbols used for transformation are

$$\tau = \frac{\alpha \Delta t}{\Delta x^2} \tag{19}$$

$$\alpha = \frac{k}{\rho C_p} \tag{20}$$

Using this transient model, temperature profiles during ramping and to a steady state point were developed for each refractory, as depicted by Figures 5 and 6, and Figures 9 and 10. It can be noted by Figure 8 that steady state in the pyro-log is achieved much faster than in the firebrick. This is likely due to the significantly lower thickness of the material layer.

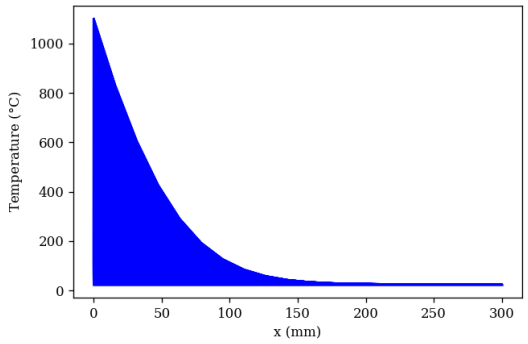

Figure 5: Firebrick temperature profile during ramping

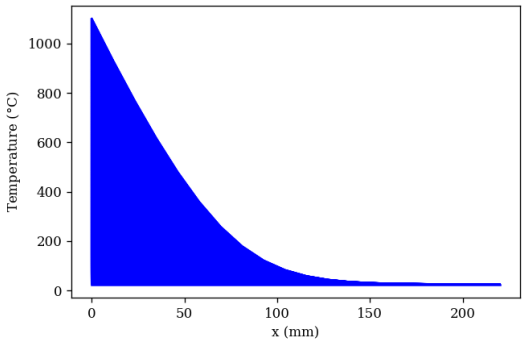

Figure 6: Pyro-log temperature profile during ramping

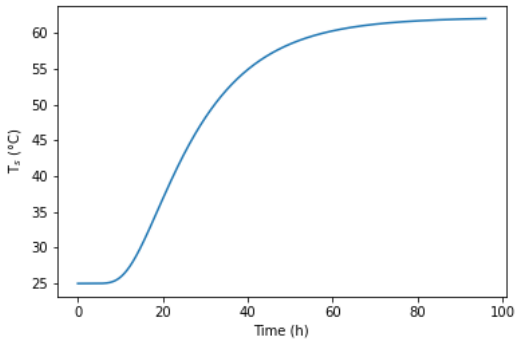

Figure 7: Firebrick external wall temperature over 96 h, to steady state

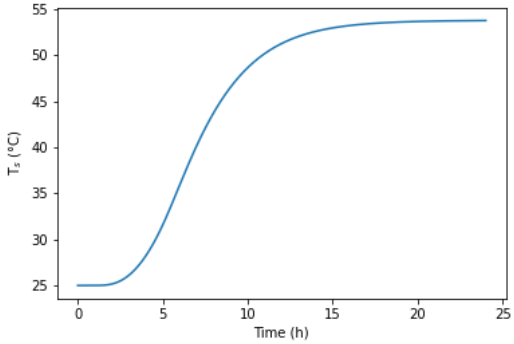

Figure 8: Pyro-log external wall temperature over 24 h

3.2.4 Heating duty

The heating duty for the furnace has been calculated based on treating each of the elements within the furnace (sample, SiC partitions and stainless steel pot) as lumped systems, such that the element uniformly reaches the furnace temperature. As such the duty required to heat these elements is

$$Q = mC_p\Delta T = \rho V C_p(T_{1100^\circ C} - T_{25^\circ C}) \tag{21}$$

The duty lost to the environment through the refractories is calculated during the transient modelling, during ramping, as the summation of Q^i (heat flux at time step i) over

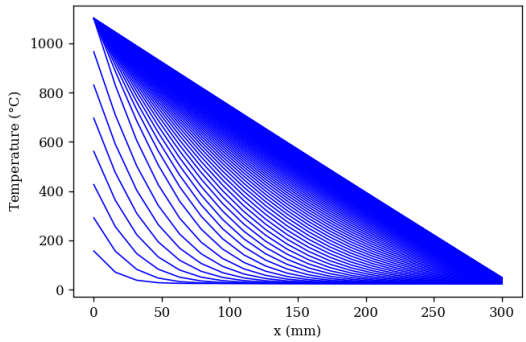

Figure 9: Firebrick temperature profile over 96 h, to steady state

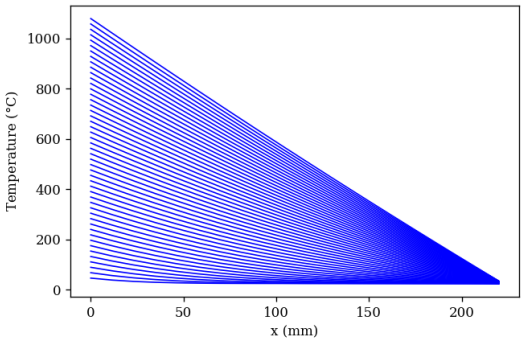

Figure 10: Pyro-log temperature profile over 24 h

the ramping period, as given by

$$Q_{refractory} = \sum_{t} Q^i \tag{22}$$

$$Q^i = -\frac{A_{wall}}{w_{wall}} \int_{T^i_{internal}}^{T^i_{external}} k(T)\mathrm{d}T \times \Delta t \tag{23}$$

where T^i represents the temperature of the internal and external wall at every time step respectively. The subsequent duties for each element of the furnace is given below

Table 5: Furnace components heating duty & mass

Component	Mass (kg)	Duty (MJ)	Power (kW)
Firebrick to air	1394	10.33	0.72
Pyro-log to air	51.6	1.99	0.14
310 Stainless steel pot & lid	16.7	9.13	0.63
SiC partitions	28.9	27.78	1.93
Sample	10.0	12.87	0.89
Total		62.10	4.31

It should be noted that the total power given in Table 5 does not represent the total power draw that the furnace will consume, as the heat absorbed by refractories still needs to be accounted for. This having been said, there is a larger loss from the firebrick to the environment to 1.51 kW when it reaches steady state, so the variation between actual operation that reported in Table 5 will not be sufficient to negatively impact furnace operation.

3.3 Mechanical design

3.3.1 Physical structure

The principal objective of a furnace is to achieve controlled heating of a product at higher temperature and lower fuel consumption than could be achieved in the open air. Most furnaces today consist of a steel outer structure with a heat resistant lining. The advantages of a steel casing compared to a brick structure reinforced with steel include:

- Reduced gas and air leakage.
- Reduced maintenance cost and complexity.
- Improved safety.
- Greater design flexibility.

When considering the use of bricks as the refractory lining, as opposed to a monolithic or ceramic fibre lining, there are certain conventions adopted that are key to the increased efficiency of the furnace. Figure 11 depicts how bricks are commonly lain in an alternating layers such that all joints are staggered. The joints are staggered so that there is no sight path between the hot gas side to the shell. Furthermore, the friction between the surfaces of the bricks is used to maintain the wall's stability (Mullinger & Jenkins, 2013).

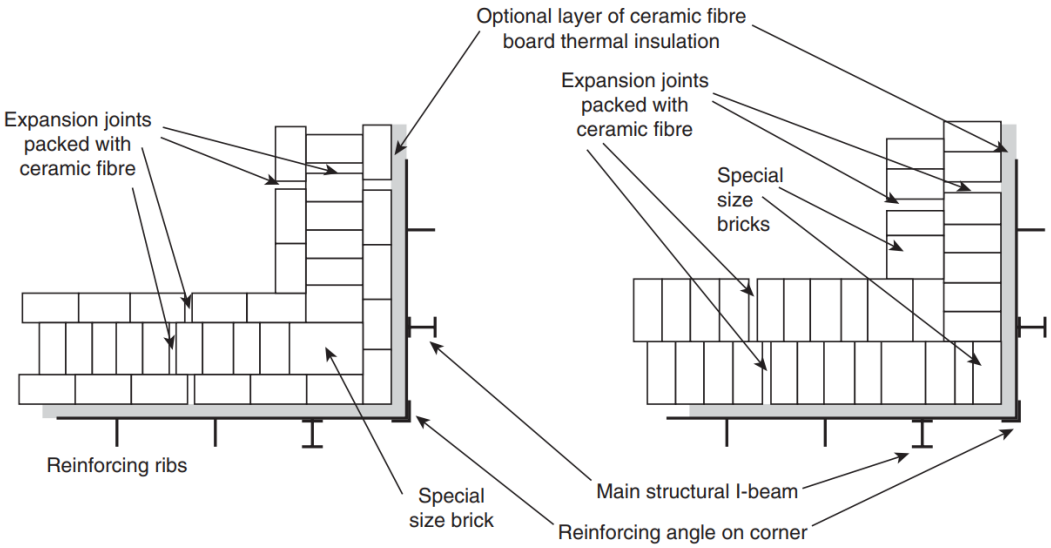

Figure 11: Typical brick lining construction (Mullinger & Jenkins, 2013)

Additional to this, expansion joints need to be provided at regular intervals to avoid overstressing the bricks at elevated temperature. Similarly, these joints are staggered to

prevent hot gas reaching the steelwork. Typically, these joints can be left as gaps, or packed with a ceramic fibre.

The refractories to be installed in the roof of the furnace require a slightly different fitment approach. Morgan Advanced Materials (2019) suggests and provide for a number of solutions, as depicted in Figure 12. Another alternative exists in fabricating and installing the required fixture beams in-house. This, however, is inevitably a finer point determined more by cost implications than anything else.

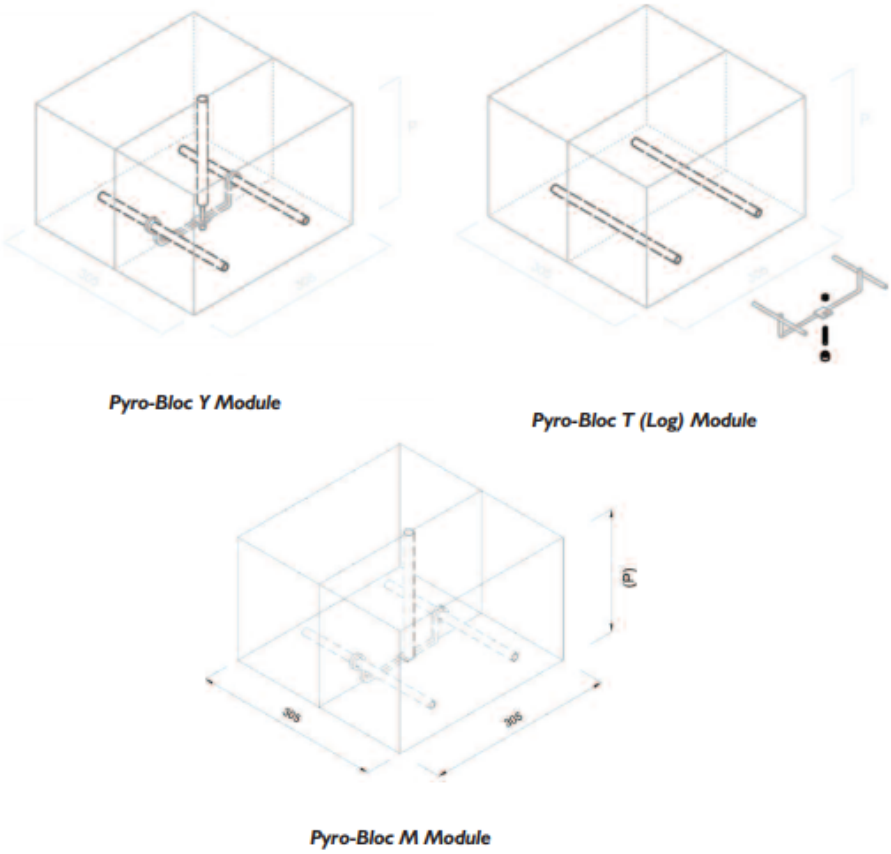

Figure 12: Typical roof refractory fitment solutions (Morgan Advanced Materials, 2019)

With regards to the steel frame itself, and its support structure, there are a number of options available. Specifically, when considering the joints of plates that form the frame, a welded or bolted approach can be adopted. While welding incurs a greater capital investment due to the increased complexity and subsequent skilled professional required, it poses the more attractive option. This is due to the undesirable behaviour expected of a bolted joint given that thermal expansion would occur in the separate plates, bolts and joining bracket or device at different rates. Furthermore, that a seal would be required between the joints, increasing the complexity of the design.

To ensure that the furnace is level when it is installed at the University of Pretoria, a design concession needs to be made given that the floor of the pilot plant workshop it is

intended to be built in is not perfectly level. One possible solution to this is to replace one of the legs with a threaded bolt sufficiently large to support the weight, enabling adjustment on the fly to level the furnace. However, given that the total load to be supported by the structure is approximately 1.4 tons, based on the mass of refractories needed, it is likely that an elegant solution is not so readily available and an alternative approach will have to be considered.

3.3.2 Instrumentation & control

Given that the planned batch furnace is intended as a test unit to gather process insight, understanding and develop models, it is crucial that sufficient data be captured from the furnace. It is thus key that provisions be made in the design for instrumentation for this data capture as well as for control purposes.

To this end, temperature measurements are of principal importance. Hence in Figure 13, the placement of numerous thermocouples is considered. For the control of the furnace, two thermocouples (referred to as temperature transmitters in Figure 13) are used, TT-01 and TT-11. TT-01 is the thermocouple used directly for control, while TT-11 is intended as a backup to serve as a fail-safe measurement device.

Thermocouples TT-02 through TT-10 are intended to record useful temperature data at various points in the furnace and crucible. TT-03, -04 and -06 are used to collect data in the radial direction of the crucible while TT-05 to TT-08 collect data in the axial direction. These should help develop understanding of the temperature profile into the pot, which can be used for optimisation of design and development of a suitable thermal model. TT-05 is to be used to obtain data on any possible cold spots that are present at the centre of the base of the crucible. The final three thermocouples, TT-02, -09 and -10 are intended to collect data on the furnace environment's temperature profile as it develops.

Please also note that Figure 13 is only intended to depict the placement of the various thermocouples and not to serve as a schematic for their physical wiring.

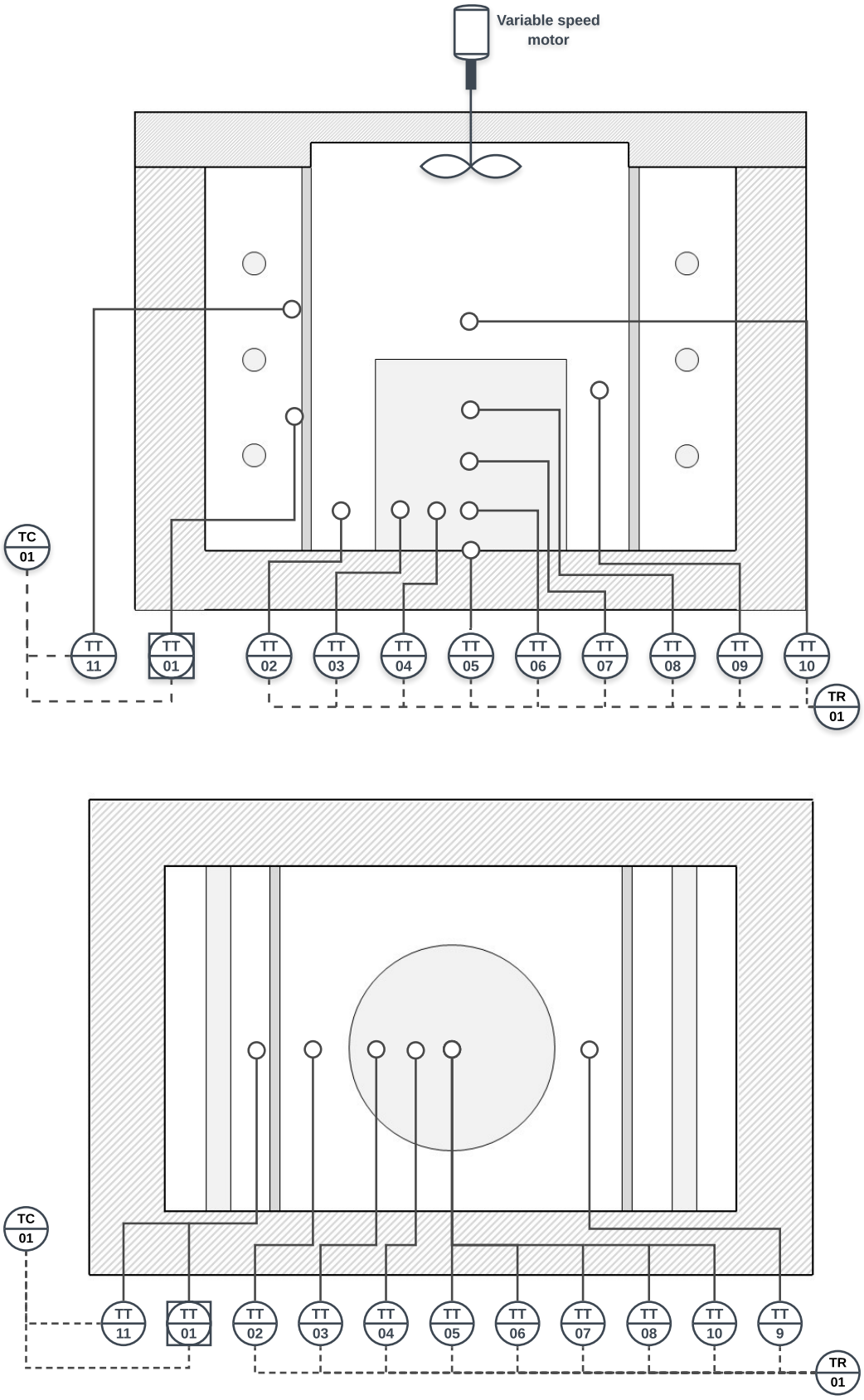

Figure 13: Preliminary furnace thermocouple placement

4 Crucible model

4.1 Model components

The scope of the model has been limited from describing the entire furnace and all the involved conductive, convective, and radiant heat transfer to rather focus on the heat transfer within the reacting material contained in the furnace. Additionally, the feed of interest has also been limited to a mixture of phosphogypsum and coal.

4.1.1 Internal heat transfer

Heat transfer is modelled using a two-dimensional finite difference approach — in the radial direction of a symmetric slice of the crucible. Figure 14 depicts the square mesh used to describe the reaction volume, as well as the assumed heat sources being from the side and top.

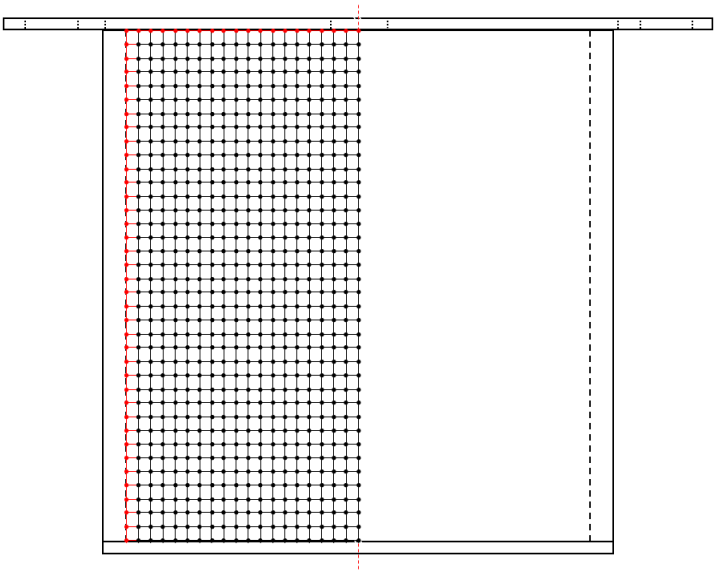

Figure 14: Crucible mesh layout and boundary description

As in Section 3.2.3, Çengel & Ghajar (2015) and Welty *et al* (1969) describe the formulation of the transient model, beginning with the energy balance on a volume element, as

$$\Delta t \times \sum_{\text{All sides}} \dot{Q} + \Delta t \times \dot{e}_{\text{element}} = \Delta E_{\text{element}} \tag{15}$$

where the rate of heat transfer, $\dot{Q}$, consists of conduction terms for the neighbouring nodes. Noting that $\Delta E_{\text{element}} = \rho C_p \Delta T$, the derivation with respect to the r and z

directions and time is

$$\frac{1}{r}\frac{\partial}{\partial r}\left(kr\frac{\partial T}{\partial r}\right)+\frac{\partial}{\partial z}\left(k\frac{\partial T}{\partial z}\right)+\dot{e}_{\text{element}}=\rho C_p\left(\frac{\partial T}{\partial t}\right) \tag{24}$$

Dividing by k throughout gives

$$\frac{1}{r}\frac{\partial}{\partial r}\left(r\frac{\partial T}{\partial r}\right)+\frac{\partial}{\partial z}\left(\frac{\partial T}{\partial z}\right)+\frac{\dot{e}_{\text{element}}}{k}=\frac{\rho C_p}{k}\left(\frac{\partial T}{\partial t}\right) \tag{25}$$

which, after simplification and noting that $\alpha = k/\rho C_p$ gives

$$\frac{\partial^2 T}{\partial r^2}+\frac{1}{r}\left(\frac{\partial T}{\partial r}\right)+\frac{\partial^2 T}{\partial z^2}+\frac{\dot{e}_{\text{element}}}{k}=\frac{1}{\alpha}\left(\frac{\partial T}{\partial t}\right) \tag{26}$$

Using the finite-difference method to approximate the partial derivatives, noting that the volume element centred around a general interior node (m,n) involves heat conduction from four sides (right, left, top, and bottom), then yields

$$\begin{aligned}&\frac{T^i_{m-1,n}-2T^i_{m,n}+T^i_{m+1,n}}{\Delta r^2}+\frac{1}{r}\left(\frac{T^i_{m+1,n}-T^i_{m-1,n}}{2\Delta r}\right)\\ &+\frac{T^i_{m,n-1}-2T^i_{m,n}+T^i_{m,n+1}}{\Delta z^2}+\frac{\dot{e}_{m,n}}{k}=\frac{1}{\alpha}\left(\frac{T^{i+1}_{m,n}-T^i_{m,n}}{\Delta t}\right)\end{aligned} \tag{27}$$

Taking a square mesh ($\Delta r = \Delta z = l$) and multiplying throughout by $\alpha\Delta t$

$$\begin{aligned}&\frac{\alpha\Delta t}{l^2}\left(T^i_{m-1,n}+T^i_{m,n-1}-4T^i_{m,n}+T^i_{m+1,n}+T^i_{m,n+1}\right)\\ &+\frac{\alpha\Delta t}{2rl}\left(T^i_{m+1,n}-T^i_{m-1,n}\right)+\frac{\alpha\Delta t}{k}\dot{e}_{m,n}=T^{i+1}_{m,n}-T^i_{m,n}\end{aligned} \tag{28}$$

Using $\tau = \alpha\Delta t/l^2$ for the final transformation then gives

$$\begin{aligned}T^{i+1}_{m,n}=\tau(T^i_{m-1,n}+T^i_{m,n-1}+T^i_{m+1,n}+T^i_{m,n+1})+(1-4\tau)T^i_{m,n}\\ +\frac{\tau l}{2r}(T^i_{m+1,n}-T^i_{m-1,n})+\tau\frac{\dot{e}_{m,n}l^2}{k}\end{aligned} \tag{29}$$

which, rewriting in a simpler-to-read form, the explicit formulation for an internal node

is given by

$$T_{node}^{i+1} = \tau(T_{left}^{i} + T_{bottom}^{i} + T_{right}^{i} + T_{top}^{i}) + (1-4\tau)T_{node}^{i} + \frac{\tau l}{2r}(T_{right}^{i} - T_{left}^{i}) + \tau\frac{\dot{e}_{\text{node}}l^2}{k} \tag{30}$$

To satisfy the insulated boundary conditions, the boundary nodes are treated as internal nodes with a fictional node set equal to the node preceding the boundary, as demonstrated in Figure 15.

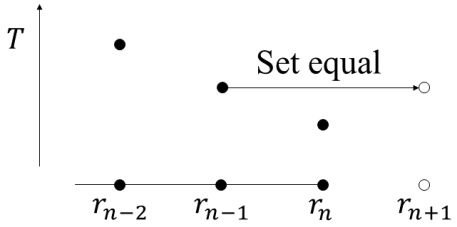

Figure 15: Illustration of an insulated boundary condition with a fictional node r_{n+1} (or z_{m+1}) with $T_{n+1} = T_{n-1}$

However, as r approaches zero (vertical side boundary condition) an accommodation for Equation 29 is required, which can be achieved by applying the limit as r approaches zero of Equation 26 as

$$\lim_{r\to 0}\left[\frac{\partial^2 T}{\partial r^2} + \frac{1}{r}\left(\frac{\partial T}{\partial r}\right) + \frac{\partial^2 T}{\partial z^2} + \frac{\dot{e}_{\text{element}}}{k}\right] = \lim_{r\to 0}\left[\frac{1}{\alpha}\left(\frac{\partial T}{\partial t}\right)\right] \tag{31}$$

$$\lim_{r\to 0}\left[\frac{\partial^2 T}{\partial r^2}\right] + \lim_{r\to 0}\left[\frac{1}{r}\left(\frac{\partial T}{\partial r}\right)\right] + \lim_{r\to 0}\left[\frac{\partial^2 T}{\partial z^2}\right] + \lim_{r\to 0}\left[\frac{\dot{e}_{\text{element}}}{k}\right] = \lim_{r\to 0}\left[\frac{1}{\alpha}\left(\frac{\partial T}{\partial t}\right)\right] \tag{32}$$

where, the only term affected by the limit, $\frac{1}{r}\left(\frac{\partial T}{\partial r}\right)$, requires the application of L'Hopitals rule

$$= \lim_{r\to 0}\left[\frac{\partial T}{\partial r}\right] \Big/ \lim_{r\to 0}[r] \tag{33}$$

$$= \lim_{r\to 0}\left[\frac{\partial^2 T}{\partial r^2}\right] \Big/ \lim_{r\to 0}[1] \tag{34}$$

$$= \frac{\partial^2 T}{\partial r^2} \tag{35}$$

thus the equation for the side boundary condition (following the same transformations as

above) is

$$2\frac{\partial^2 T}{\partial r^2} + \frac{\partial^2 T}{\partial z^2} + \frac{\dot{e}_{\text{element}}}{k} = \frac{1}{\alpha}\left(\frac{\partial T}{\partial t}\right) \tag{36}$$

$$\frac{2T^i_{m-1,n} - 4T^i_{m,n} + 2T^i_{m+1,n}}{\Delta r^2} + \frac{T^i_{m,n-1} - 2T^i_{m,n} + T^i_{m,n+1}}{\Delta z^2} + \frac{\dot{e}_{m,n}}{k} = \frac{1}{\alpha}\left(\frac{T^{i+1}_{m,n} - T^i_{m,n}}{\Delta t}\right) \tag{37}$$

$$T^{i+1}_{m,n} = \tau(2T^i_{m-1,n} + T^i_{m,n-1} + 2T^i_{m+1,n} + T^i_{m,n+1}) + (1-6\tau)T^i_{m,n} + \tau\frac{\dot{e}_{m,n}l^2}{k} \tag{38}$$

which, again, rewriting in a simpler-to-read form, the explicit formulation for the side boundary node is given by

$$T^{i+1}_{node} = \tau(2T^i_{left} + T^i_{bottom} + 2T^i_{right} + T^i_{top}) + (1-6\tau)T^i_{node} + \tau\frac{\dot{e}_{\text{node}}l^2}{k} \tag{39}$$

4.1.2 Reaction kinetics

In addition to the heat transfer, the reaction kinetics are modelled. The reaction and conversion of species present is described by the kinetic model proposed by Kato *et al* (2012). It is suggested that the reaction follows

$$\mathrm{CaSO_4} + 2\mathrm{C} \longrightarrow \mathrm{CaS} + 2\mathrm{CO_2} \tag{40}$$

$$3\mathrm{CaSO_4} + \mathrm{CaS} \longrightarrow 4\mathrm{CaO} + 4\mathrm{SO_2} \tag{41}$$

and, assuming that each rate can be expressed by first-order reaction with respect to $\mathrm{CaSO_4}$, CaS, and C concentrations in the solid phase, the mass balances for the components can be given by

$$\frac{\mathrm{d[CaSO_4]}}{\mathrm{d}t} = -k_1[\mathrm{CaSO_4}][\mathrm{C}] - 3k_2[\mathrm{CaSO_4}][\mathrm{CaS}] \tag{42}$$

$$\frac{\mathrm{d[CaS]}}{\mathrm{d}t} = k_1[\mathrm{CaSO_4}][\mathrm{C}] - k_2[\mathrm{CaSO_4}][\mathrm{CaS}] \tag{43}$$

$$\frac{\mathrm{d[CaO]}}{\mathrm{d}t} = 4k_2[\mathrm{CaSO_4}][\mathrm{CaS}] \tag{44}$$

$$\frac{\mathrm{d[C]}}{\mathrm{d}t} = -2k_1[\mathrm{CaSO_4}][\mathrm{C}] \tag{45}$$

The rate constants, k_1 and k_2, can be expressed using the Arrhenius equation

$$k_i = k_{i(0)}\exp\left[-\frac{E_i}{RT}\right] \tag{46}$$

where the kinetic parameters fit by Kato *et al* (2012) for a heating rate of 10 °C min^{-1} are $k_{10} = 3.2 \times 10^{15}$ mol^{-1} s^{-1}, $E_1 = 370$ kJ mol^{-1}, $k_{20} = 1.6 \times 10^{15}$ mol^{-1} s^{-1}, and $E_2 = 400$ kJ mol^{-1}.

Using the heating rate and constants given, a plot of the species against time for any given number of moles of reaction can be obtained, as shown in Figure 16. This can be used to determine the composition of the mixture at any given time during the simulation.

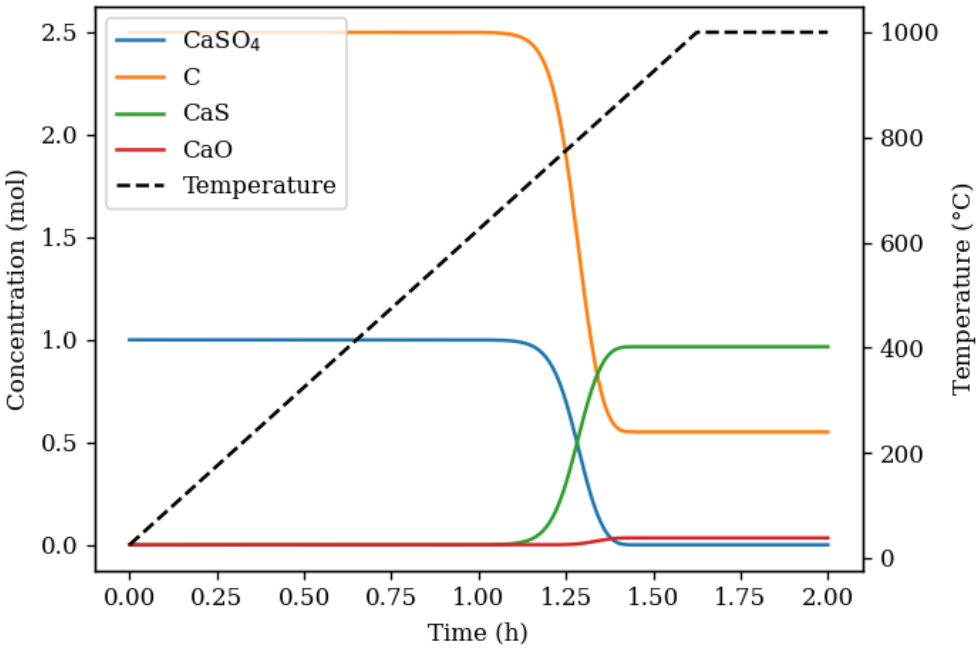

Figure 16: Kinetic profile of the carbothermal reduction of 1 mole of $CaSO_4$

4.1.3 Heat of reaction

Equation 29 include a heat generation term that constitutes the heat of reaction of the reduction. Roine (2018) gives the heat of reaction at 1000 ° C as 153.4 kJ mol^{-1}. Using the volume of a node and the change in number of moles of $CaSO_4$ between consecutive time steps (equivalent to moles of reaction), the heat of reaction can be calculated in the discretisation as

$$\dot{e}^{i}_{\text{node}} = \frac{\Delta n_{\text{CaSO}_4} \Delta H_{rxn}}{\Delta t V_{\text{node}}} \tag{47}$$

4.1.4 Combined implementation

A number of assumptions have been made for the modelling process, and are as follows:

1. The reaction species form a perfect, uniformly distributed mixture
2. Heat generation is calculated using a constant heat of reaction at 1000 °C (as the heat of reaction at 800 °C is only 4.8 % larger)
3. Concentrations of reaction species are determined using the discretised kinetics — for each node individually
4. The thermal conductivity (k) of the mixture is calculated using a volume-fraction based average of the initial amounts of phosphogypsum and coal charged and kept constant thereafter
5. The heat capacity (C_p) of the mixture is calculated using a simple mass-fraction based average of the components present for a node at any given time
6. It is assumed the reacting mass does not contract
7. The bulk density (ρ_B) of the mixture has been measured experimentally as 836 kg m^{-3} and is varied according to the mass loss as the reduction proceeds
8. Heat transfer properties (C_p, ρ_B, α, and τ) are calculated for each node every iteration at the temperature of the node
9. The model does not include gangue material (ash and volatiles in coal and impurities in phosphogypsum)
10. Heat losses to the bottom of the crucible are neglected

As indicated by point 4, the thermal conductivity is a constant over the simulation, calculated using the thermal conductivity of phosphogypsum, 0.43 W m^{-1} K^{-1} (though has been given to range between 0.43–0.51 W m^{-1} K^{-1}), (Bejan, 2013; Green & Perry, 2008; Tesárek *et al*, 2007) and coal, 0.26 W m^{-1} K^{-1} (Bejan, 2013; Green & Perry, 2008), and the initial bulk volume fractions of phosphogypsum, 0.74, and coal, 0.26. Using Equation 48, this gives a k_{mix} of 0.377 W m^{-1} K^{-1}.

Furthermore, as per point 5 above, the overall model accounts for changes in the material composition using the reaction kinetics and incorporates these changes as the properties (C_p, and ρ_B which affect α, and τ) used in the heat transfer part of the modelling. While

the heat capacity is calculated using a simple mass-fraction based (or volume-based in the case for k) average, given by

$$M_{mix} = \sum_{components} M_i \times fr_i \tag{48}$$

the bulk density is varied with the mass loss caused by the reaction assuming the volume of the reacting mass stays constant.

4.2 Modelling procedure & constraints

The explicit heat transfer equations described in Section 4.1.1 form the core of model, with the reaction accounted for by varying the heat transfer properties (C_p, ρ_B, α and τ) as per the reaction kinetics and as the heat of reaction term from the enthalpy of reaction.

As the kinetics are heavily dependent on the initial concentrations or mass of reactants charged, the kinetics are simulated in the discretisation along with the heat transfer. This enables the model to accurately correlate the degree of conversion of any given node and calculate the subsequent heat transfer properties. The heat of reaction term is similarly calculated for each iteration.

Heat is introduced to the system by uniformly ramping the temperature of the outside nodes (top and side as per Figure 14) according to a set heating rate from 25 °C and then holds the temperature at the maximum of 1000 °C, once it is reached, for the remainder of the simulation.

Using the originally envisioned 300 by 300 mm crucible, with a charged mass of 15 kg and a heating rate of 10 °C min^{-1}, to exemplify these concepts, the reaction can be shown to occur very similarly to the 1-mol case (Figure 16) for a single node, but with a slightly delayed profile, as depicted by Figure 17. This kinetic profile manifests in the changes to the heat transfer properties and their influence on the Fourier mesh number, τ (Figure 18), used in Equation 29. Although the shape of the curves in Figure 18 is dependent on the rate of reaction, it will follow the same general trend where the positive linear increase of the C_p of the reactants with temperature undergoes a rapid change as the reactants are converted to the products as the reaction initiation temperature is reached. It should be noted that the thermal conductivity is not varied during this simulation due to the limited literature available.

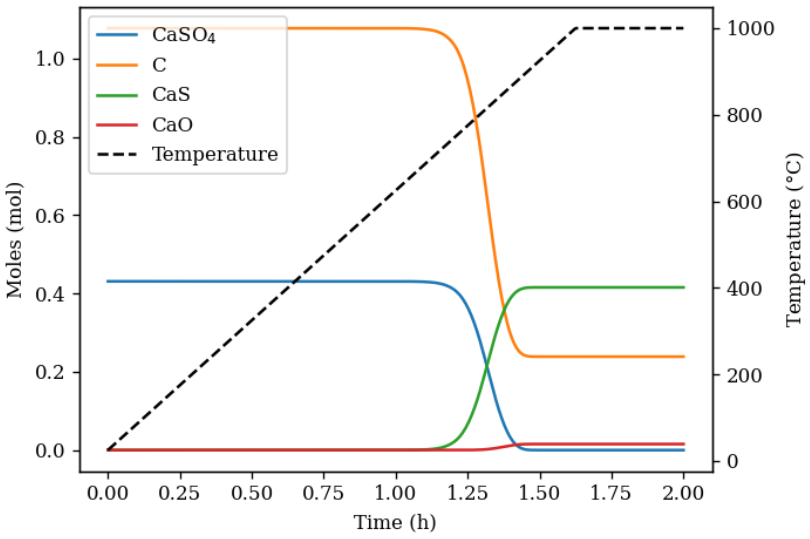

Figure 17: Kinetic profile for a single node in the reduction of 15 kg of gypsum and coal mixture

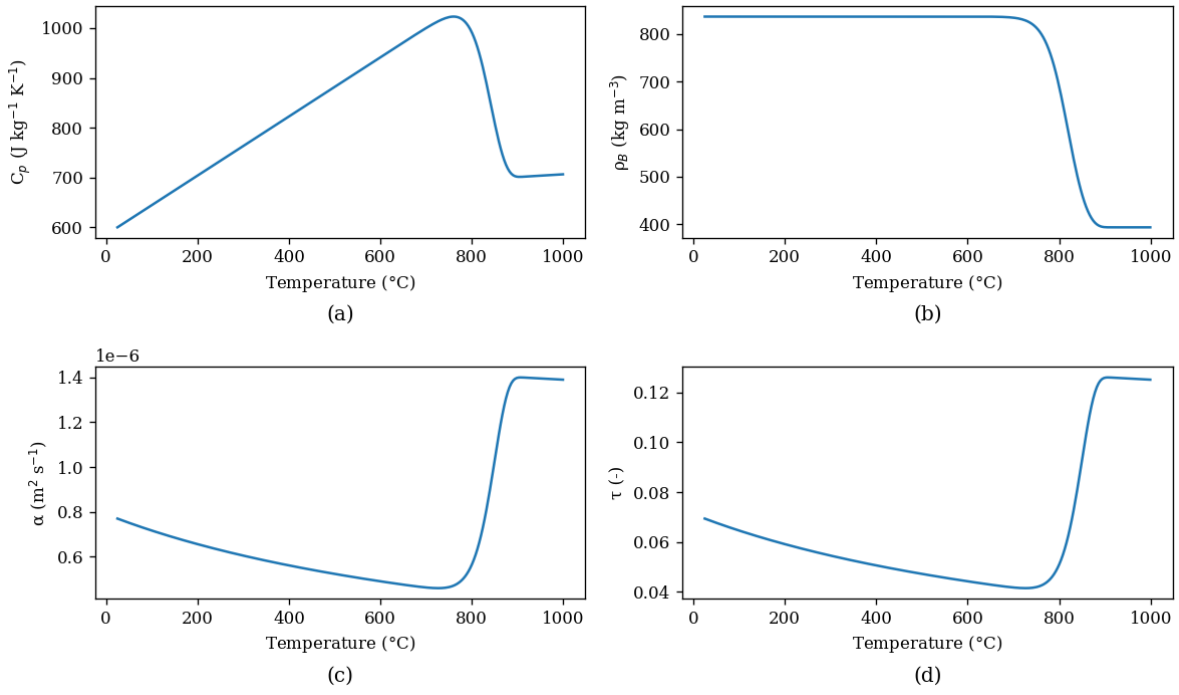

Figure 18: (a) $C_{p_{mix}}$; (b) $\rho_{B_{mix}}$; (c) α_{mix}; (d) τ_{mix} over the reaction temperature range

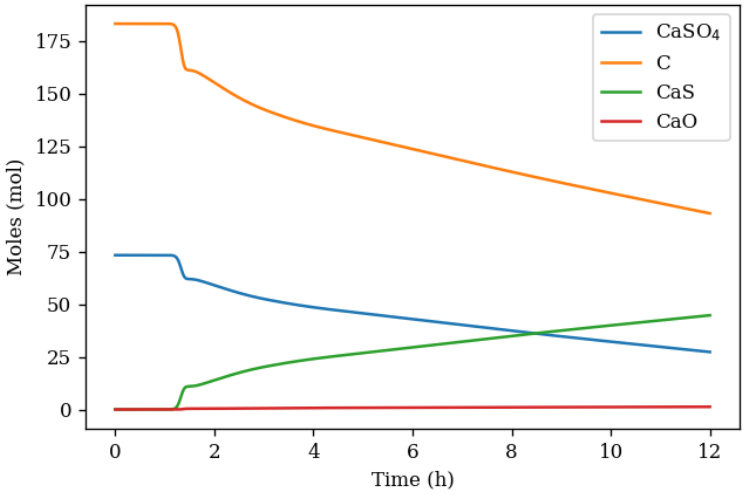

Figure 19: Kinetic profile for the overall reduction of 15 kg of gypsum and coal mixture over 12 h

The simulation of the reacting mixture begins with the square mesh (as in Figure 14) initialised to 25 °C throughout. The exterior boundary (top and side) temperatures are then ramped according to the given heating rate each iteration. Each iteration also progresses the heat through the mesh by applying Equation 29, with appropriate changes to the heat transfer properties according to Equation 48 once the reaction initialisation temperature has been reached. The overall product curve, Figure 19, shows the progressive product evolution due to the heat progression towards the centre-bottom of the vessel. The sharp spike before 2 h is due to the reaction at the boundary nodes (and likely those immediately adjacent) occurring rapidly due to their ramping temperature.

The simulation culminates in a progressive heating of the mixture towards the centre-bottom of the crucible, as can be seen by Figure 20.

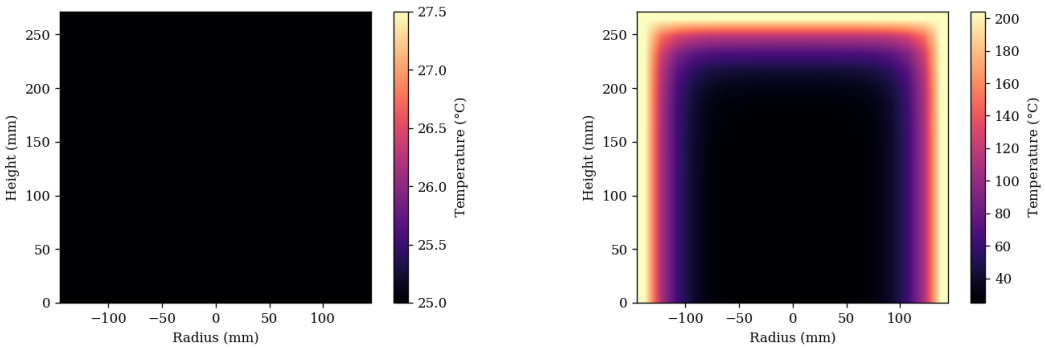

(a) 0 min **(b)** 15 min

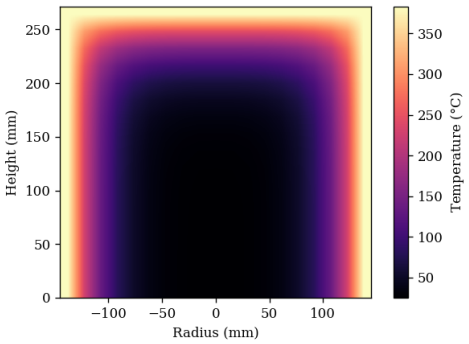

(c) 30 min

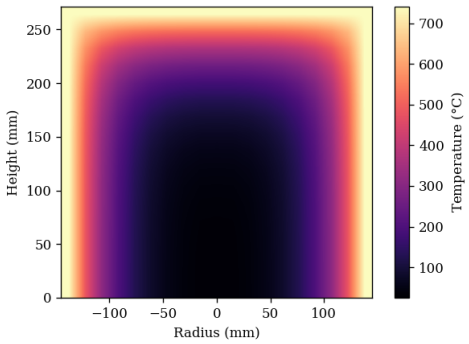

(d) 1 h

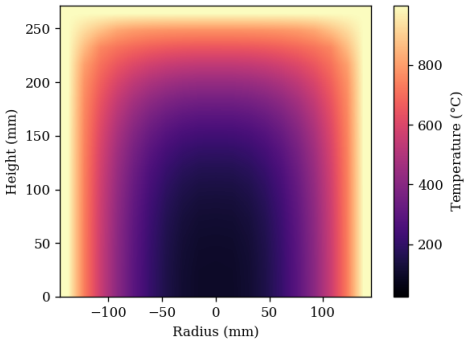

(e) 2 h

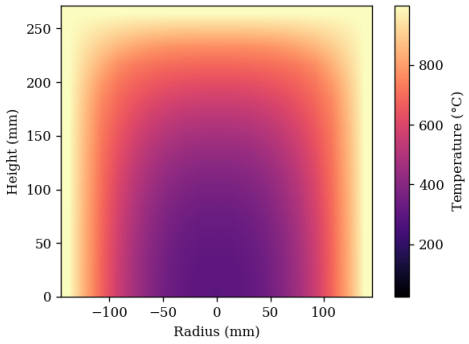

(f) 4 h

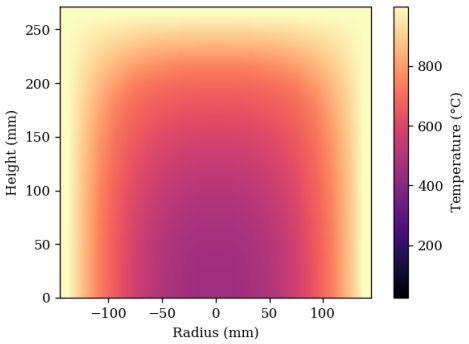

(g) 6 h

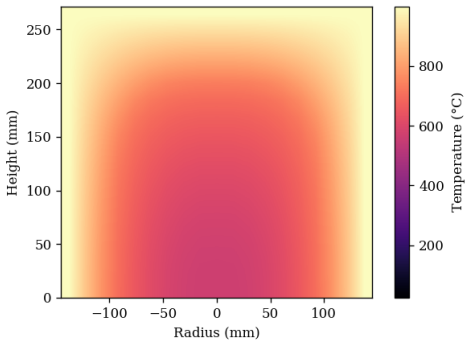

(h) 8 h

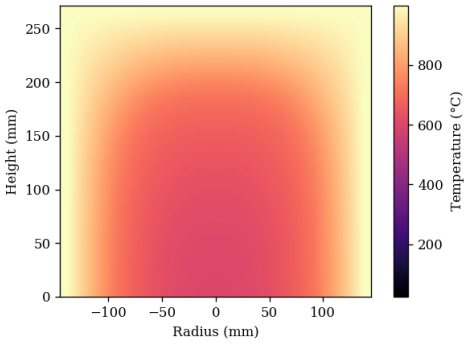

(i) 9 h

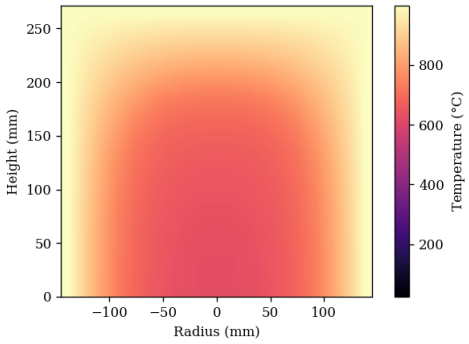

(j) 10 h

Figure 20: Heatmap progression for a 15 kg sample over 10 h

5 Experimental

5.1 Materials

For the purposes of both sizing the batch furnace and determining the mass and energy balances for the process, phosphogypsum, sourced from Foskor, with a compositional analysis as given in Table 6 and a heat capacity of 1090 J kg^{-1} K^{-1} (Engineering ToolBox, 2003c; Manzello *et al*, 2008; Prieler *et al*, 2018), was used along with coal, with a proximate analysis as given in Table 7 and a heat capacity of 1380 J kg^{-1} K^{-1} (Engineering ToolBox, 2003c; Tomeczek & Palugniok, 1996; van Krevelen, 1961).

Table 6: Phosphogypsum composition (dehydrated)[1] (Oberholzer & Nel, 2020)

Species	Mass %
SiO_2	1.61
Al_2O_3	0.0325
Fe_2O_3	0.14
TiO_2	0.008
CaO	37
MgO	0.135
Na_2O	0.0935
K_2O	0.075
MnO	0.0015
H_3PO_4	1.760495
BaO	0.039079
Cr	0.0035
Cu	0.0025
Ni	0.0035
Pb	0.001
SrO	0.396173
V	<0.001
Zn	<0.001
CO_2	0.071453
SO_3	54.05579
Moisture	0.83
Loss on ignition	6.39

[1] Phosphogypsum was first dehydrated at 300 °C for 6 h

Table 7: Coal proximate analysis (air dried) (Oberholzer & Nel, 2020)

Item	Value	Units
Calorific value	26.49	MJ kg^{-1}
H_2O	2.70	
Ash	16.10	
Volatile matter	24.8	Mass %
Fixed carbon	56.4	
Total sulphur	0.453	

5.2 Apparatus

The presented furnace & subsequent crucible could not be constructed due to a delay in funding from the project sponsor, therefore, two in-house-made stainless steel crucibles were used in a medium sized muffle furnace to perform the experiments. Both three- and six-inch diameter vessels were made using 310 stainless steel and had holes drilled through the lid to allow thermocouples to be placed in various locations to capture the temperature profile of the reacting mixture. Figure 21 below depicts the thermocouple layout for the crucibles.

5.3 Analytical instruments

Product samples were analysed using a PANalytical X'Pert Pro powder diffractometer in σ–σ configuration with an X'Celerator detector and variable divergence- and fixed receiving slits with Fe filtered Co-Kα radiation ($\lambda = 1.789$Å). The mineralogy was determined by selecting the best–fitting pattern from the ICSD database to the measured diffraction pattern, using X'Pert Highscore plus software. The relative phase amounts (weight %) were estimated using the Rietveld method (X'Pert Highscore plus).

The samples were prepared according to the standardised PANalytical back-loading system, which provides nearly random distribution of the particles.

5.4 Planning

The experiments were designed around obtaining the temperature profile of the reacting mixture so as to adequately validate the developed model. Four experiments were performed, maintaining the heating rate (3 °C min^{-1}), maximum temperature (1000 °C), nitrogen purge gas flow rate (1 L min^{-1}) and reactant composition uniformly throughout

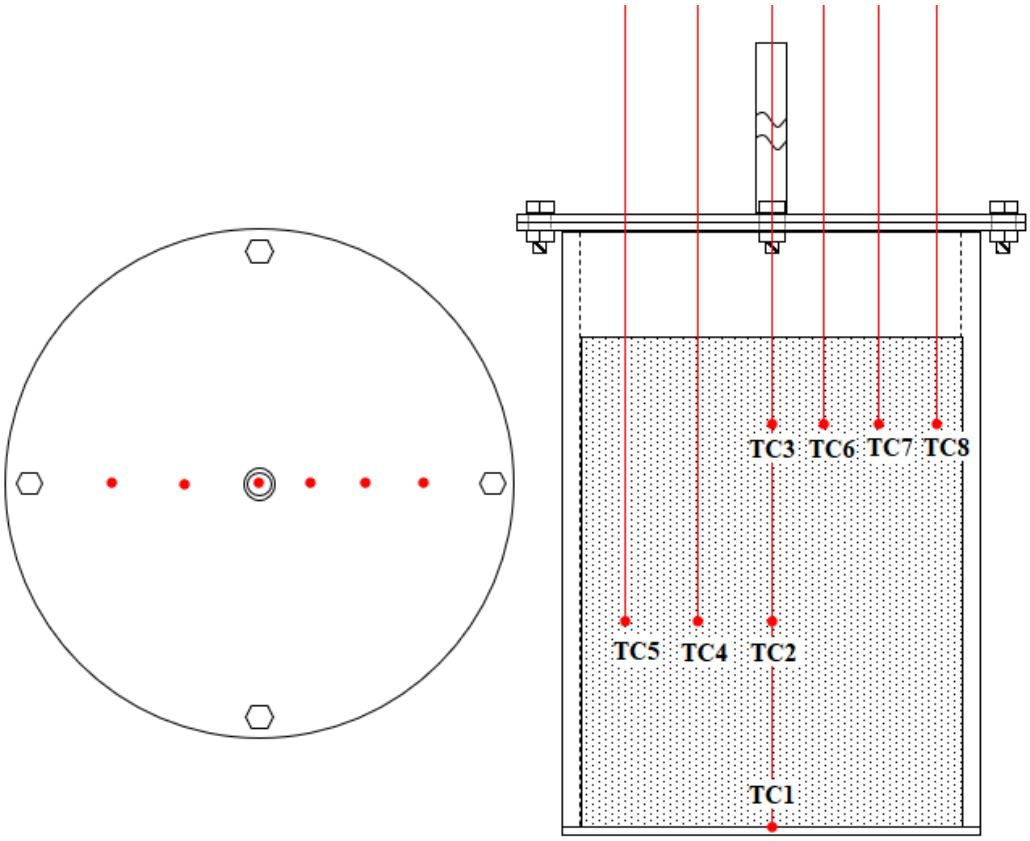

Figure 21: Thermocouple layout within crucible

(0.35-coal : 1-phosphogypsum (dehydrated) so as to obtain 2.5C : 1$CaSO_4$). Variances in the mass loading for the respective crucibles is detailed in Table 8 below.

Table 8: Experiment description

Experiment	Crucible diameter	Mass loaded (g)
1	3-inch	350
2	3-inch	400
3	3-inch	500
4	6-inch	2000

It should be noted that in trial experiments using higher heating rates, the purge gas feed caused reactant material blow-out from the crucible due to the fineness of the powder and the purge gas' rapid flow rate increase with temperature. This issue was also prevalent in lower heating rates but could be mitigated with appropriate adjustments to the purge gas' inlet positioning.

A number of type-K thermocouples were placed so as to capture temperature profiles at various heights and radial distances from the centre, these positions are described in Table 9 and are graphically represented by Figure 21.

Table 9: Thermocouple positioning

Thermocouple	3-inch crucible		6-inch crucible	
	DFC[1] (mm)	DFB[2] (mm)	DFC (mm)	DFB (mm)
TC1	0	0	0	0
TC2	0	70	0	70
TC3	0	120	0	120
TC4	19.4	70	33.6	70
TC5	34	70	62	70
TC6	16	120	26	120
TC7	26.6	120	47.2	120
TC8	37.8	120	68.4	120

[1] Distance from centre
[2] Distance from bottom

6 Results and discussion

6.1 Experimental results

XRD analysis suggests a very high extent of conversion with no $CaSO_4$ present in the product samples, and a CaS content varying from 90–93 wt-% (Table 10). Trace amounts of CaO were also detected, these findings indicate that the reaction occurred as expected, with the primary reduction to CaS dominating the side reaction producing CaO.

It should be noted that excess carbon is present in the samples, however the peaks overlap with that of quartz, which is present as an impurity from both the phosphogypsum and coal (Figures 22 and 23).

Table 10: Relative phase amounts determined from XRD analysis

Experiment number	Oldhamite (CaS) %	Quartz (SiO_2) %	Apatite-(CaF) %	Lime (CaO) %
1	92.76	2.3	4.8	0.13
2	93.46	2.13	4.41	-
4	90.38	1.98	7.64	-

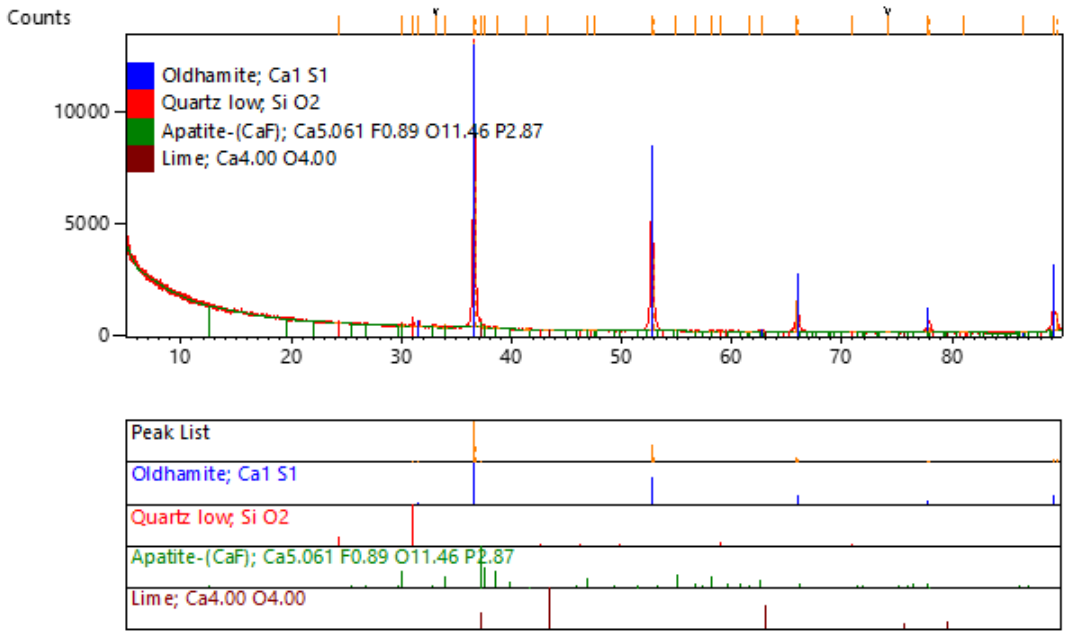

Figure 22: XRD results for a mass charge of 350 g

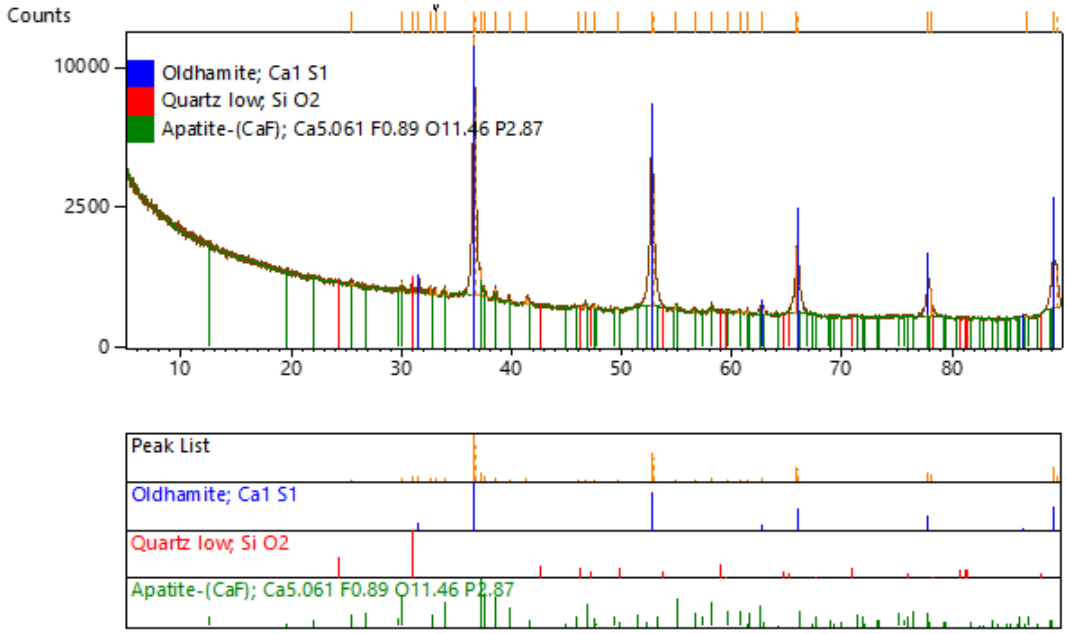

Figure 23: XRD results for a mass charge of 2000 g

6.2 Model validation

The model was validated by comparing the temperature profiles of the embedded thermocouples with the equivalent position model-node's profile.

The mass load in the three-inch crucible was varied with intent to see whether a noticeable difference in the centre-bottom temperature profile could be seen by varying the area available for heat transfer within a constrained environment. The mass load in the six-inch crucible was kept constant and served to investigate the effect scaling has on the heat transfer. When looking at the model results presented in Table 11, it can be seen that, although the model lags behind the experimental results, a general trend, where the additional mass causes an increase in the amount of time to reach 1000 °C, is present.

Table 11: Centre-bottom node final temperatures

Mass load (g)	Model		Experiment	
	Time to T_f (h)	T_f (°C)	Time to T_f (h)	T_f (°C)
350	10.3	1000	5.5	984
400	11.0	1000	6.48	999
500	11.9	1000	6.5	1006
2000	15.1	1000	9.78	997

Considering Figure 24, as can be seen by the behaviour of TC1, TC2, TC4 and TC5 in the 350, 450 and 500 g experiments, the increase in height results in slightly delayed profiles as those nodes become more deeply embedded in the material. The 2000 g experiment's packed bed is of similar height to the 500 g case, but with a much larger crucible diameter, subsequently the more embedded nodes' profiles are much more delayed in reaching 1000 °C. The intermediate plateaus of the more embedded nodes are likely due to endothermic contribution of the heat of reaction of the more exterior nodes causing a delay or dead-time in the transfer of heat as well as the endothermic effects of the node itself counteracting the heating.

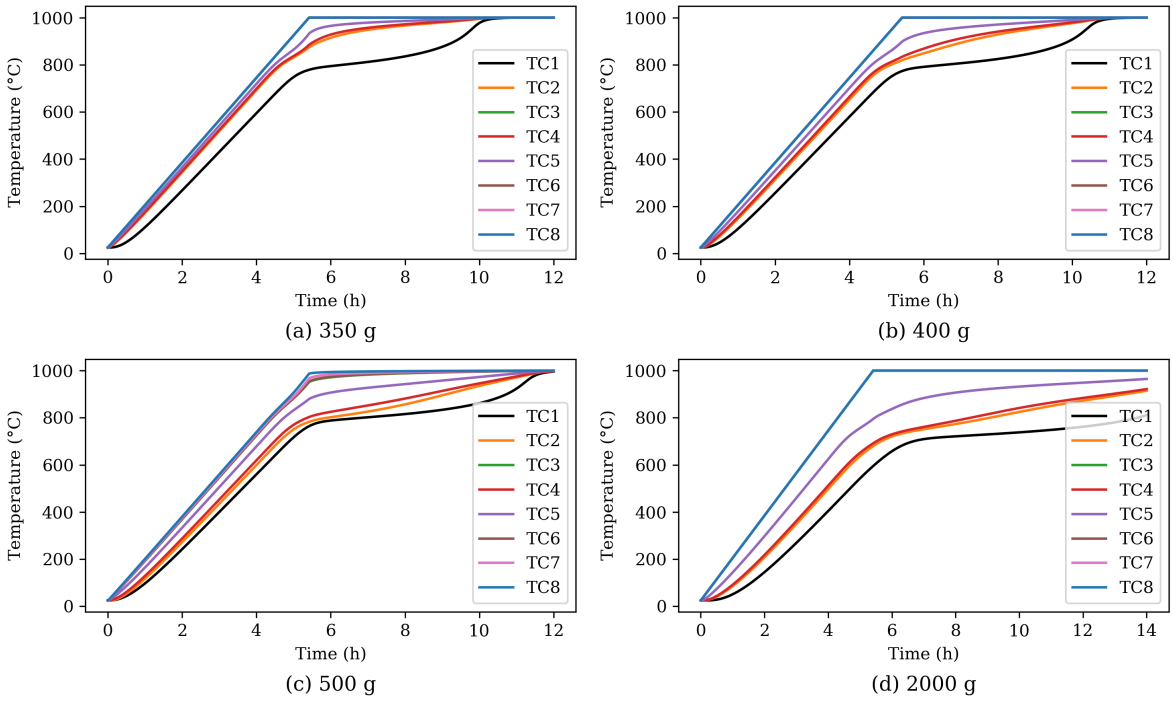

Figure 24: Node temperature profiles for (a) 350 g; (b) 400 g; (c) 500 g; (d) 2000 g

Comparing experimental results to those predicted by the model, Figure 25 shows that the model overestimates the time to final temperature, especially for the nodes more towards the centre bottom. Furthermore, as can be seen over the course of increasing the mass, the model's degree of inaccuracy increases with the increasing mass of material and vessel diameter. This suggests a number of possibilities: that the estimated thermal conductivity is too low, as the experimental nodes all experience faster heating than the model predicts; or that the kinetic parameters presented by Kato *et al* (2012) are not an accurate representation for the coal and gypsum used in these experiments and are under-predicting the rate of reaction.

Although the model achieves conservative results, which can be useful in industrial practice, it is clear there is room for improvement. Section 6.3 investigates the possible shortfalls of the model presented above.

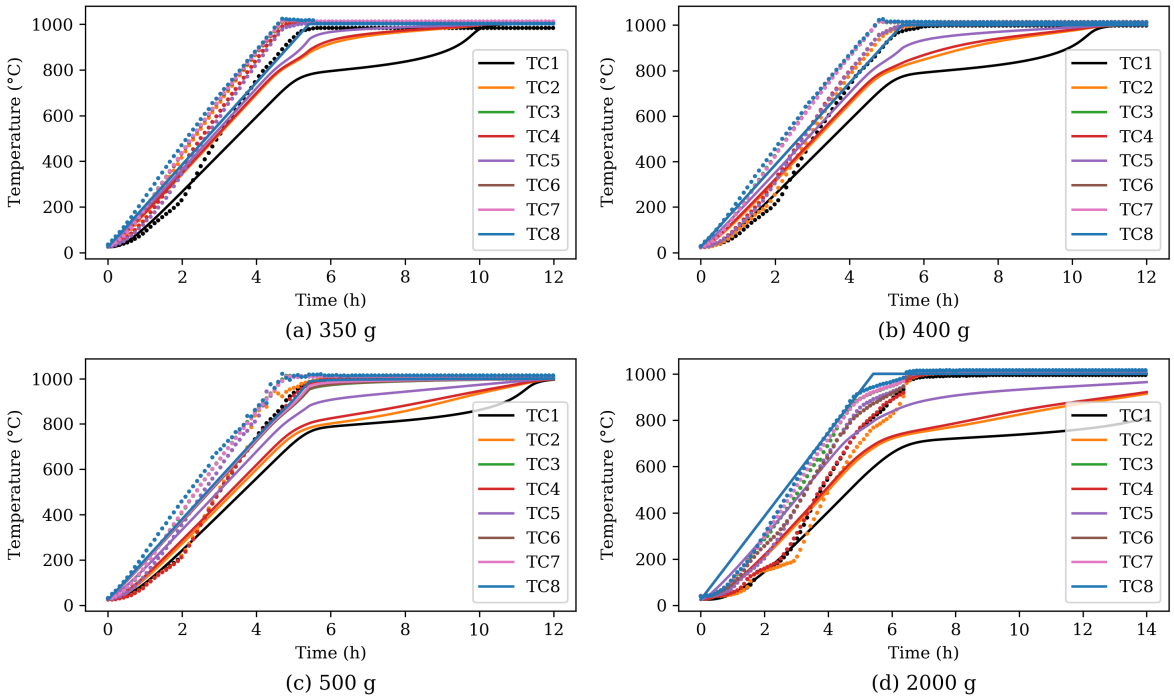

Figure 25: Experimental and model temperature profile comparison for (a) 350 g; (b) 400 g; (c) 500 g; (d) 2000 g, where dotted lines indicate experimental data

6.3 Model sensitivity analysis

By varying the pre-exponential factor of the reduction of gypsum or thermal conductivity of the system, their accuracy for the model can be evaluated.

Figure 26, which compares the 500 g experimental case, shows that increasing the rate of reaction does not have a pronounced effect on the model's overall accuracy. Although, it should be noted that the time taken for a node to reach the final temperature was decreased, but not substantially.

The work by Godbee & Ziegler (1966), Laubitz (1959), and Luikov *et al* (1968) on the thermal conductivity of powder beds and porous systems shows that values for k can vary between 0.2 W m^{-1} K^{-1} at 25 °C and 1 W m^{-1} K^{-1} at 1000 °C for a variety of different powders. This is used as a basis for the variation of the k values in the model. As can be seen by Figure 27, the increase in thermal conductivity results in a significantly closer representation of the experimental data when compared to the base case ($k = 0.377$) and the increased rate of reaction cases (Figure 26). This suggests that the thermal conductivity plays a more substantial role in determining the heating of the vessel than the rate of the reaction does.

It should be noted, however, that a constant value for k is not necessarily an accurate representation, hence Figure 28 below, depicts the effects of having the thermal conduc-

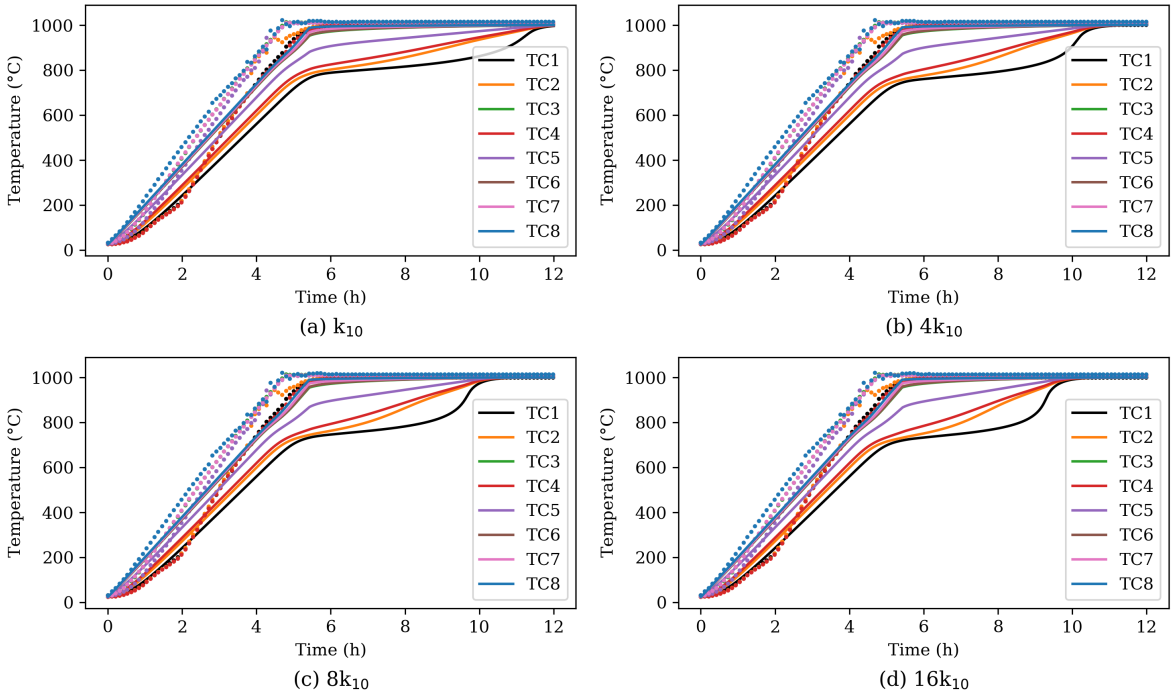

Figure 26: Effect of increasing pre-exponential factor for (a) k_{10}; (b) $4k_{10}$; (c) $8k_{10}$; (d) $16k_{10}$, where dotted lines indicate experimental data

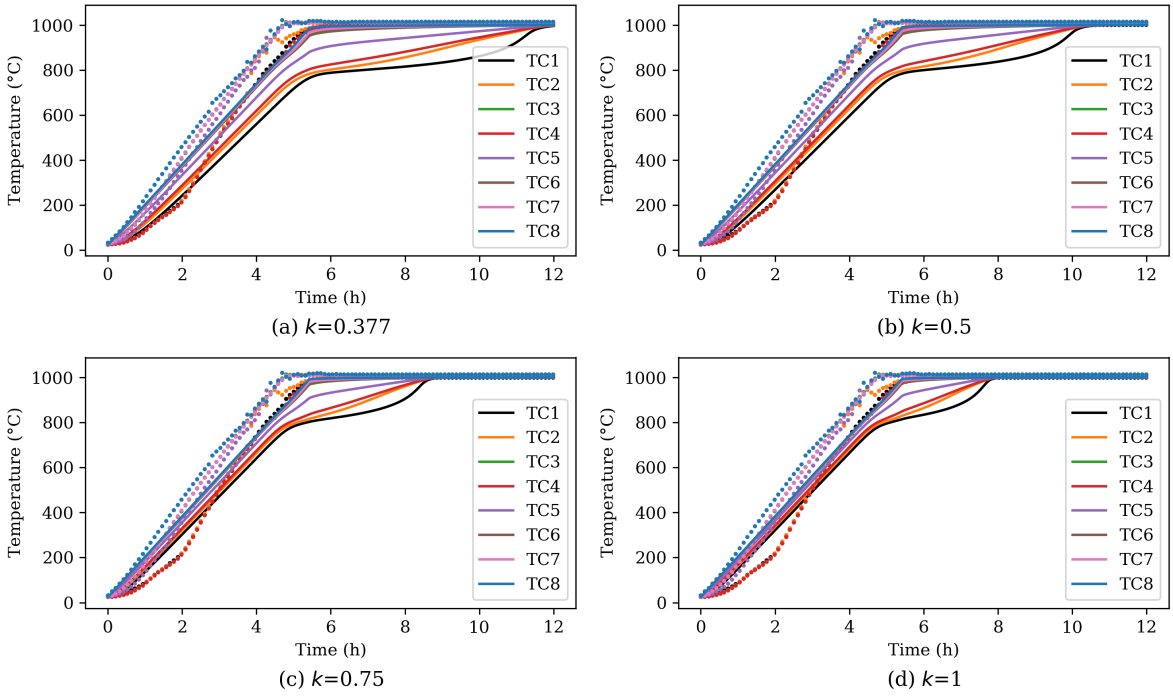

Figure 27: Effect of increasing (constant) thermal conductivity for (a) $k = 0.377$; (b) $k = 0.5$; (c) $k = 0.75$; (d) $k = 1$, where dotted lines indicate experimental data

tivity of the system vary linearly with temperature as per Equation 49 (although Laubitz (1959) shows that powders can vary logarithmic or exponentially depending on the powder composition). Equation 49 is derived on the basis that k can be assumed to be equal to 0.377 W m^{-1} K^{-1} at 25 °C and 1 W m^{-1} K^{-1} at 1000 °C.

$$k(T) = 6.39 \times 10^{-4} T + 0.1865 \tag{49}$$

Additionally, Table 12 shows the time taken to achieve final temperature. As with the higher constant values for k, Figure 28 is a better representation of the experimental data than the base case, but still lags behind the experiments by some measure.

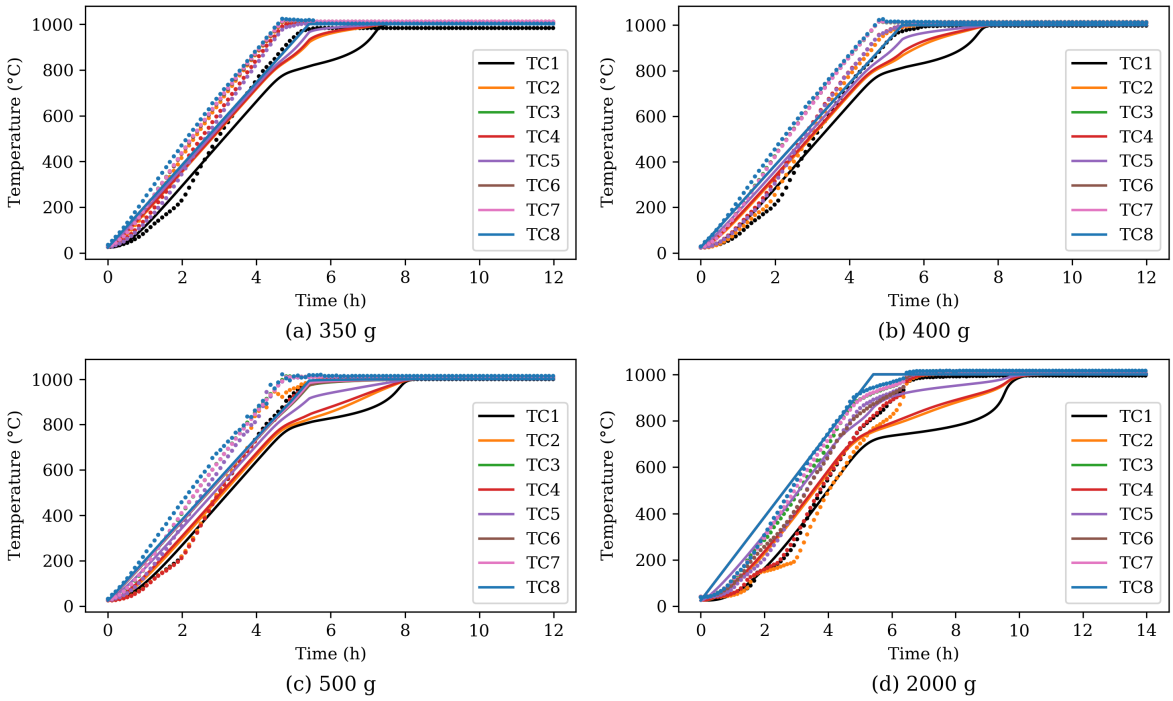

Figure 28: Experimental and model temperature profile comparison with a linearly increasing k, for (a) 350 g; (b) 400 g; (c) 500 g; (d) 2000 g, where dotted lines indicate experimental data

Table 12: Centre-bottom node final temperatures with a linearly varying thermal conductivity

Mass load (g)	Model		Experiment	
	Time to T_f (h)	T_f (°C)	Time to T_f (h)	T_f (°C)
350	7.4	1000	5.5	984
400	7.7	1000	6.48	999
500	8.1	1000	6.5	1006
2000	10.2	1000	9.78	997

The presented adjustments to the model achieve conservative results, which is useful in industrial practice, however, it is clear that there is still some inaccuracy. It is possible that there exists a convective contribution to heat transfer within the vessel, but more work is required to validate that. Furthermore, it would still be beneficial to investigate whether the heat transfer limitations have a greater effect on experiments conducted in larger vessels with larger masses, as it is clear from the data obtained that, at the scale and the rate of heating tested, the heat transfer limitations are not very pronounced.

6.4 Proposed tunnel kiln optimisation

The model can also be used to perform a sensitivity analysis to predict the effect vessel size has on any given mass. Testing a range of masses (100–300 kg) and vessel sizes (0.4–1.4 m), using the model with a linearly varying with temperature k term, and a heating rate of 10 °C min^{-1}, a simulation over 48 h yields the results as shown in Figure 29. This sensitivity analysis was used to see which configurations achieved at least 950 °C (when the reaction will be well underway) within the 48 h and how long it took to achieve that.

The time taken for the centre-bottom nodes to reach 950 °C is depicted in Figure 30, and as can be expected, there exists a trend that a more shallow material bed achieves temperature faster (with the height sometimes preventing temperature being reached at all).

Unrealistically tall vessels, and unsuitably thin material beds were not included and are represented by a "nan" term in the figures (with acceptable heights falling within 20–300 % of the vessel diameter). Shallow beds were not included as this analysis is limited to cylindrical vessels, and a configuration where the material heating is primarily dominated by the top layer would be better suited to a cubic/rectangular loading (as the mass loading can be 21.5 % greater). The upper limit of the height of vessels and their loading was set to a factor of three of the vessels' diameter for structural stability reasons.

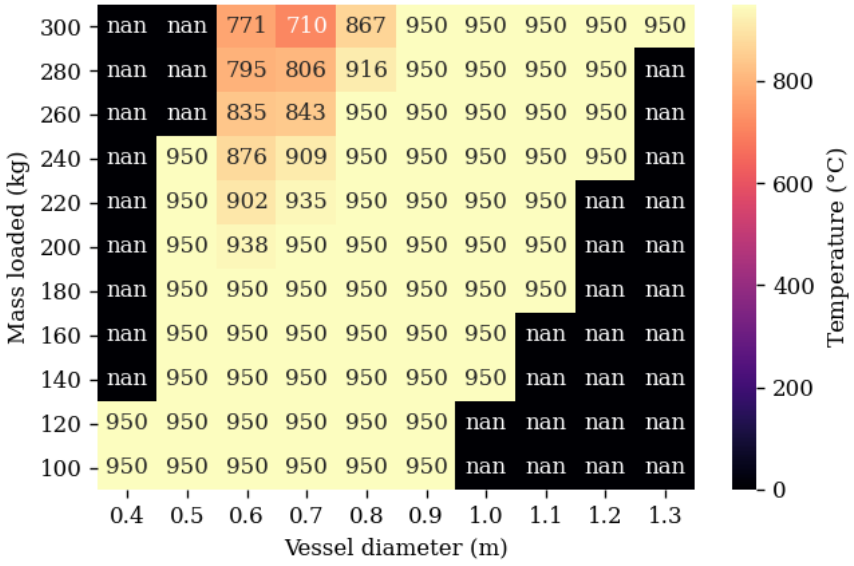

Figure 29: Centre-bottom node final temperatures, where "nan" indicates a null value due to an unsuitable configuration

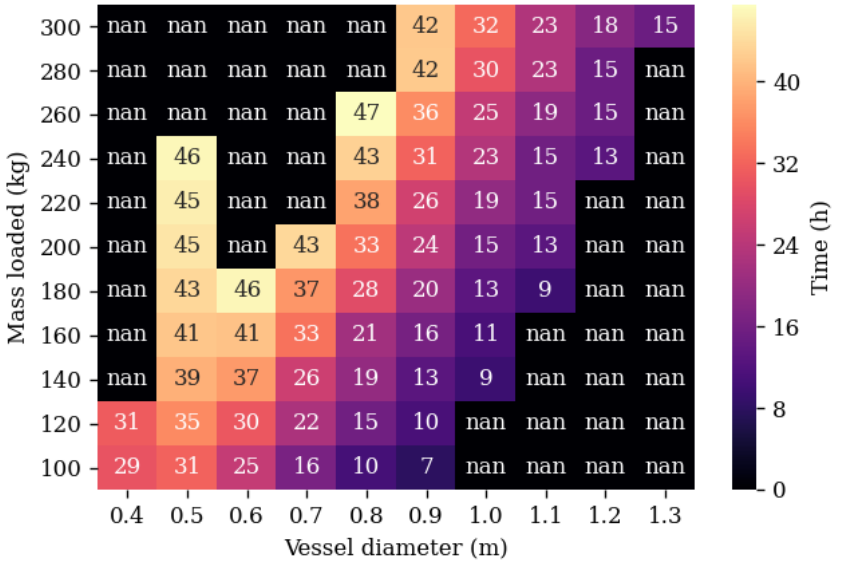

Figure 30: Time to reach final temperature, where "nan" indicates a null value due to an unsuitable configuration or a centre point not having reached 950 °C

Using several patents for the direct reduction of iron in a tunnel kiln as a basis, the dimensions for a hypothetical-tunnel kiln have been set as 4 m × 4 m × 100 m (W × H × L) (Hauxing, 2012; Qingfeng, 2005; Xinzheng, 2020; Yicheng, 2014; Zhongji, 2012). This can be used to estimate a material processing rate. Given the amount of time to reach 950 °C, the residence time in the furnace (with interest limited to the

heating and holding at temperature only and not cooling) can be calculated and used to estimate a throughput for each configuration assuming full conversion. Full conversion in this context implies a feed of pure reactants converting fully to products (with additional excess carbon) whereby 1 kg feed yields approximately 0.47 kg product. It should be noted that the number of vessels is maximised for each configuration by stacking multiple layers on top of each other and side by side. Additionally, only 80 % of the available area was utilised to allow for sufficient space between vessels and the walls/roof and consecutive kiln cars.

As per Figure 31, it can be seen that the optimum is a shallow bed (on the edge of the imposed limit on bed height) and a production rate of 771 Mt per year is predicted. This value is a bit large, with direct iron reduction tunnel kilns processing between 100–500 Mt per year (Qingfeng, 2005), but could be achievable. It should be noted that these results are not incontestable due to the inaccuracies in the model and how said inaccuracies tend to increase with a larger mass and vessel diameter (as seen in Section 6.2). Furthermore, as indicated above, it would be beneficial to investigate the throughput of square or rectangular shallow depth trays compared to cylindrical vessels.

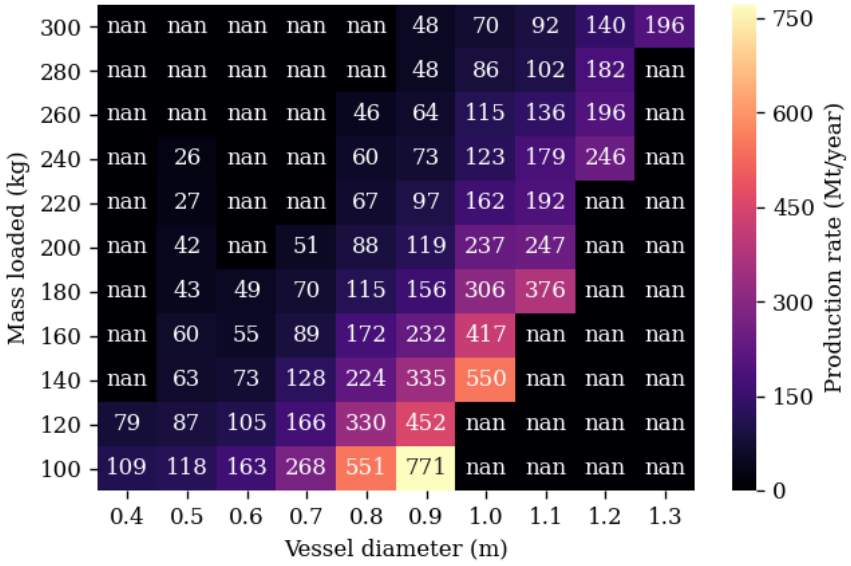

Figure 31: Material processing rate, where "nan" indicates a null value due to an unsuitable configuration or a centre point not having reached 950 °C

7 Conclusions

Phosphogypsum waste represents a potential source for the recovery of elemental sulphur, rare earth elements, and calcium carbonate. With focus given to the reducing step of

the process, converting the sulphates to sulphides, there is good precedence shown that the reduction of phosphogypsum can be achieved by means of carbothermal reduction. Coal should serve as a suitable source of carbon for the process step, with coal's ready availability and relatively low cost being key factors in its choice.

The reduction of calcium sulphate occurs within a temperature range of 850–1100 °C. Additionally, an unfavourable secondary reaction producing calcium oxide initiates at 900 °C. However, this side reaction is an oxidative reaction, and sufficient excess carbon charged with the feed serves to mitigate the negative impact on sulphide yield.

It is generally held that the primary reducing agent during the reduction is a gaseous intermediate, and furthermore that the presence of O_2 and CO_2 are undesirable as they favour the production of calcium oxide and calcium sulphate. It is recommended that, for the use of coal as carbonaceous material, an environment that favours excess amounts of CO in the kiln should be created to carry out the reduction.

The addition of catalysts such as ferric oxide or potassium dichromate can enhance the reaction satisfactorily and reduce the initiation temperature to approximately 750 °C and increase the sulphide yield. However, an economic study into the cost versus increased yield would naturally be a necessary requirement when considering commercial application.

Sodium sulphate can be reduced within the temperature range of 700–900 °C, with the temperature of initiation depending strongly on the reducing agent used and the presence of catalysts. The reaction poses significant difficulties, primarily with the formation of a eutectic between sodium sulphate and sodium sulphide. Furthermore, the reaction mixture becomes very corrosive (due to the sodium sulphide), and strongly attacks the lining of the furnace and crucible it is held in. The reduction of sodium sulphate was of secondary interest in this study, as similar technology to the reduction of calcium sulphate might be applied if a suitable material of construction for the crucible can be found.

The purification of the resulting products also pose difficulties, as the Na_2S generally contains excess carbon, ash components, Na_2CO_3, $Na_2S_2O_3$, and Na_2SO_3. The reactor product can either be leached with water or a solution of methanol. The method making use of methanol obtains a product that is free of water, iron, sulphite, sulphate and thiosulphate, unlike the product that is leached using water.

Lime is suggested as a catalyst for sodium sulphate reduction when using coal, and the use of catalysts for this reaction should be strongly considered, given that formation of the eutectic can be avoided by reducing the initiation temperature sufficiently.

The model presented describes the heat transfer within a reacting bed of phosphogypsum and coal by means of a two-dimensional transient finite difference method. The scope of the model has been limited from describing the entire furnace & all the involved conductive, convective, and radiant heat transfer to rather focus on the heat transfer within the reacting material contained in the vessels within the furnace.

The kinetics of the reaction is used to estimate the development of products as heating occurs and the subsequent composition of a node in the finite difference model. This change in composition is taken into account by means of adjusting the heat transfer properties (C_p, α and τ) used in the heat transfer calculation for each node respective to its temperature.

The model is validated against experimental data, using two different reaction vessels, a three-inch and a six-inch crucible. Each vessel contains several thermocouples placed to capture various position's temperature profile. The vessels were heated to 1000 °C with a heating rate of 3 °C min^{-1} while purging with nitrogen gas.

The model achieves conservative results, over-predicting the time required to reach 1000 °C. It can be noted that the variation of pre-exponential factor for the reaction has a substantially less significant effect than the variation of the thermal conductivity of the system. This indicates that the thermal conductivity values available from literature (which are limited) do not sufficiently describe the system. It would be beneficial to study the thermal conductivity to enable a more accurate representation of the system. Application of a linearly varying with temperature thermal conductivity in the model achieves reasonable results and matches the trends observed in experimental results well. However, it is still recommended that larger scale experiments be conducted as the model shows an increasing inaccuracy as the mass and vessel diameter increased.

A sensitivity analysis for a hypothetical tunnel kiln is used to determine the optimum cylindrical vessel configuration to maximise the possible material processing rate. The analysis found that a shallower material bed results in a more optimal setup, with more efficient heat transfer. This results in an estimated production rate of 771 Mt per year. However, the design of a furnace is a complicated process with many variables, so these results are far from conclusive and it is recommended to determine whether a shallow square/cubic configuration is better suited.

The model has good flexibility and can be updated and improved readily. Conservative results indicate a good applicability for the model in industrial scenarios where factors of safety are necessary. The model shows good suitability for the prediction of the heat transfer occurring within a reacting bed of solid phosphogypsum and coal.

8 Acknowledgements

The author would like to extend thanks to the Department of Trade, Industry and Competition of South Africa for sponsoring the project, ROC Water for their part in managing the project, and Foskor for making phosphogypsum available for use for the experiments performed.

9 References

Akah, A (2017) "Application of rare earths in fluid catalytic cracking: A review" *Journal of Rare Earths*, *35*, 941.

Anval Valves (2019) *Bulk Density Chart* URL: `http://www.anval.net/downloads/bulk%5C%20density%5C%20chart.pdf` (visited on 07/10/2019).

Azo Materials (2019) *Stainless Steel - Grade 310* URL: `https://www.azom.com/properties.aspx?ArticleID=966` (visited on 07/10/2019).

Bejan, A (2013) *Convection Heat Transfer*, 4th ed. John Wiley & Sons.

Binmaster (2019) *Bulk Density Chart* URL: `https://www.binmaster.com/_resources/dyn/files/75343622z9caf67af/_fn/Bulk%5C%20Density.pdf` (visited on 07/10/2019).

Birk, J, Larsen, C, Vaux, W and Oldenkamp, R (1971) "Hydrogen reduction of alkali sulfate" *Industrial & Engineering Chemistry Process Design and Development*, *10*, 7–13.

Brooks, MW and Lynn, S (1997) "Recovery of calcium carbonate and hydrogen sulfide from waste calcium sulphide" *Industrial & Engineering Chemistry Research*, *36*, 4236–4242.

Budnikoff, P and Shilov, E (1971) "The reduction of sodium sulfate to sodium sulfide particularly by hydrogen and carbon monoxide in the presence of catalysts" *Journal of the Society of Chemical Industry*, *6*, (4).

Cameron, J and Grace, T (1983) "Kinetic study of sulfate reduction with carbon" *Industrial & Engineering Chemistry Fundamentals*, *22*, (4): 486–494.

Çengel, YA and Ghajar, AJ (2015) *Heat and Mass Transfer: Fundamentals & Applications*, 5th ed. McGraw-Hill, New York.

Chase, MW (1998) "NIST-JANAF Themochemical Tables, Fourth Edition" *Journal of Physical and Chemical Reference Data*, *9*, 1–1951.

Cork, DJ, Jerger, DE and Maka, A (1986) "Biocatalytic production of sulphur from process waste streams" *Biotechnology and Bioengineering*, *16*, 149–162.

Courtois, G (1939) "Sur la fusibilite des melanges de sulfure et de sulfate de sodium purs anhydres" *Comptes rendus de l'Académie des Sciences*, *208*, 199–201.

De Beer, M, Doucet, FJ, Maree, JP and Liebenberg, L (2015) "Synthesis of high-purity precipitated calcium carbonate during the process of recovery of elemental sulphur from gypsum waste" *Waste Management*, *46*, 619–627.

De Beer, M, Maree, JP, Liebenberg, L and Doucet, FJ (2014) "Conversion of calcium sulphide to calcium carbonate during the process of recovery of elemental sulphur from gypsum waste" *Waste Management*, *34*, (11): 2373–2381.

Dutta, T, Kim, KH, Uchimiya, M, Kwon, EE, Jeon, BH, Deep, A and Yun, ST (2016) "Global demand for rare earth resource and strategies for green mining" *Environmental Research*, *150*, 182–190.

Engineering ToolBox (2003a) *Classification of Coal* URL: `https://www.engineeringtoolbox.com/classification-coal-d_164.html` (visited on 07/10/2019).

Engineering ToolBox (2003b) *Convective Heat Transfer* URL: `https://www.engineeringtoolbox.com/convective-heat-transfer-d_430.html#targetText=Typical%5C%20convective%5C%20heat%5C%20transfer%5C%20coefficients,%5C%2F(m2K))` (visited on 07/10/2019).

Engineering ToolBox (2003c) *Specific Heat of Solids* URL: `https://www.engineeringtoolbox.com/specific-heat-solids-d_154.html` (visited on 07/10/2019).

Finney, KN, Sharifi, VN and Swithenbank, J (2009) "Fuel pelletization with a binder: Part II-the impacts of binders on the combustion of spent mushroom compost-coal tailing pellets" *Energy & Fuel*, *23*, 3203–3210.

Garside, M (2021) *Price of sulfur in the United States from 2014 to 2020* URL: https://www.statista.com/statistics/1031180/us-sulfur-price/#statisticContainer (visited on 05/10/2021).

Godbee, HW and Ziegler, WT (1966) "Thermal Conductivities of MgO, Al_20_3, and ZrO_2 Powders to 850 °C" *Journal of Applied Physics*, *37*, (1): 40–55.

Gorkan, A, Prada, S, Pathak, G and Kulkarni, S (2000) "Vanadium catalysed gasification of carbon and its application in the carbothermic reduction of barite" *Fuel*, *79*, 821–827.

Green, DW and Perry, RH (2008) *Perry's Chemical Engineers' Handbook*, 8th ed. McGraw-Hill, New York.

Hauxing, J (2012) "Tunnel kiln used for performing reduction reaction on iron powder", *CN203534155U*, assigned to Powder Metallurgy Technology Co. LTD, China.

Jagtap, S, Pande, A and Gokarn, A (1990) "Effect of catalysts on the kinetics of the reduction of barite by carbon" *Industrial & Engineering Chemistry Research*, *29*, 795–799.

Kale, B, Pande, A and Gokarn, A (1992) "Studies in the carbothermic reduction of phosphogypsum" *Metallurgical and Materials Transactions B*, *23*, 567.

Kato, T, Murakami, K and Sugawara, K (2012) "Carbon reduction of gypsum produced from flue gas desulfurization" *Chemical Engineering Transactions*, *29*, 805–810.

Keramicalia (2019) *High Temperature Kerasic* URL: https://www.keramicalia.co.za/castables/383-high-temperature-kerasic (visited on 07/15/2019).

Kim, BS and Sohn, HY (2002) "A novel cyclic process using $CaSO_4$/CaS pellets for converting sulfur dioxide to elemental sulfur without generating secondary pollutants: Part II. Hydrogen reduction of calcium-sulfate pellets to calcium sulfide" *Metallurgical and Materials Transactions B*, *33*, (5): 717.

Kirk-Othmer, ed. (2004) *Kirk-Othmer Encyclopedia of Chemical Technology*, 5th ed. Wiley.

Kozicki, C and Carlson, C (2020) *Phosphogypsum — An Industrial Byproduct With Value* URL: `https://feeco.com/phosphogypsum-an-industrial-byproduct-with-value/` (visited on 05/10/2021).

Kulczycka, J, Kawaski, Z, Smol, M and Wirth, H (2016) "Evaluation of the recovery of rare earth elements (REE) from phosphogypsum waste-case study of the WIZOW chemical plant (Poland)" *Journal of Cleaner Production*, *113*, 345–354.

Laubitz, MJ (1959) "Thermal Conductivity of Powders" *Canadian Journal of Physics*, *37*, 798–808.

Ley, P (1934) "Title unavailable" *Chemiker Zeitung*, *58*, 59–60.

Li and Zhuang (1999) "Catalytic reduction of calcium sulfate to calcium sulfide by carbon monoxide" *Industrial & Engineering Chemistry Research*, *38*, (9): 3333–3337.

Luikov, AV, Shashkov, AG, Vasiliev, LL and Fraiman, YE (1968) "Thermal Conductivity of Porous Systems" *International Journal of Heat and Mass Transfer*, *11*, 117–140.

Ma, L, Niu, X, Hou, J, Zheng, S and Xu, W (2011) "Reaction mechanism and influence factors analysis for calcium sulfide generation in the process of phosphogypsum decomposition" *Thermochimica Acta*, *526*, 163–168.

Macías, F, Caraballo, M and Nieto, JM (2012) "Environmental assessment and management of metal-rich wastes generated in acid mine drainage passive remediation systems" *Journal of Hazardous Materials*, *229*, 107–114.

Manzello, S, Park, SH, Mizukami, T and Bentz, D (2008) "Measurement of thermal properties of gypsum board at elevated temperatures" in: the Fifth International Conference on Structures in Fire, Singapore, May 28-30, 2008: pp. 656–665.

Mark, HF, Othmer, DF, Overberger, CG and Seaborg, GT (1978) *Kirk-Othmer: Encyclopedia of Chemical Technology*, 3rd ed. Wiley-Interscience, New York.

Mbhele, NR, Van der Merwe, W, Maree, JP and Theron, D (2009) *Recovery of sulfur from waste gypsum* In: Abstracts of the International Mine Water Conference, 19–23 October 2009, Cilla Taylor Conferences.

Miao, Z, Yang, H, Wu, Y, Zhang, H and Zhang, X (2012) "Experimental studies on decomposing properties of desulfurization gypsum in a thermogravimetric analyzer and multi-atmosphere fluidized beds" *Industrial & Engineering Chemistry Research*, *51*, 5419–5423.

Morgan Advanced Materials (2019) *Product Data Book* URL: `http://www.morganthermalceramics.com/media/5454/morgan-advanced-materials_thermal-ceramics-product-data-book-e-version_2.pdf` (visited on 07/10/2019).

Motaung, S, Zvimba, J, Maree, J and Kolesnikov, A (2015) "Thermochemical reduction of pelletized gypsum mixed with carbonaceous reductants" *Water SA*, *41*, 369.

Mullinger, P and Jenkins, B (2013) "Chapter 11 - Furnace Construction and Materials", in: *Industrial and Process Furnaces*, Mullinger, P and Jenkins, B (Eds.), 2nd ed. Butterworth-Heinemann, Oxford: pp. 415–455.

Nengovhela, NR, Strydom, CA, Maree, JP, Oosthuizen, S and Theron, DJ (2007) "Recovery of sulphur and calcium carbonate from waste gypsum" *Water SA*, *33*, 741–747.

Ning, P, Zheng, SC, Ma, LP, Du, YL, Zhang, W, Niu, XK and Wang, FY (2011) "Kinetics and thermodynamics studies on the decomposition of phosphogypsum in different atmospheres" *Advanced Materials Research*, *160*, 842–848.

Nowak, M, Jaroszek, H and Turkowska, M (2014) "Conversion of waste sodium sulfate with bipolar membrane electrodialysis", in: *Membranes and Membrane Processes in Environmental Protection*, *119*, pp. 337–348.

Nyman, C and O'Brien, T (1947) "Catalytic reduction of sodium sulfate" *Industrial & Engineering Chemistry*, *39*, (8): 1019–1021.

Oates, JAH (1986) *Lime and Limestone: Chemistry and Technology, Production and Uses*, Wiley-VCH, Verlag GmbH, Weinheim.

Oberholzer, JJ and Nel, SS (2020) *Analytical Report: Ash and Coal Samples* Analytical report 32626 UIS Analytical Services, Pretoria.

Oh, J and Wheelock, T (1990) "Reductive decomposition of calcium sulphate with carbon monoxide: reaction mechanism" *Industrial & Engineering Chemistry Research*, *29*, 544–550.

Peelman, S, Sun, ZHI, Sietsma, J and Yang, Y (2016) *Leaching of rare earth elements: Review of past and present technologies* URL: http://dx.doi.org/10.1016/B978-0-12-802328-0.000021-8 (visited on 11/20/2019).

Prieler, R, Mayrhofer, M, Eichhorn-Gruber, M, Schwabegger, G and Hochenauer, C (2018) "Development of a numerical approach based on coupled CFD/FEM analysis for virtual fire resistance tests-Part A: Thermal analysis of the gas phase combustion and different test specimens" *Fire and Materials*, *43*, (5): 34–50.

Qingfeng, Y (2005) "Tunnel kiln without exterior combustion chamber and production of direct reduced iron by composite tunnel kiln", *CN1804049A*, China.

Roine, A (2018) *HSC Chemistry* Software Outotec, Pori, Software available at URL: http://www.outotec.com/HSC.

Ruto, S, Maree, JP, Zvinowanda, CM, Louw, WJ and Kolesnikov, AV (2011) "Thermal studies on gypsum in a pilot-scale rotary kiln" in: Water in the South African Minerals Industry Conference Proceedings, White River, Mphumalanga, February, 2011.

Selim, H, Gupta, AK and Al Shoaibi, A (2013) "Effect of reaction parameters on the quality of captured sulphur in Claus process" *Applied Energy*, *104*, 772–776.

Sliger, AG (1988) "The MW Kellogg Company KEL-S Process" in: Second International Symposium on Phosphogypsum, Miami, Florida, January, 1988: pp. 83–107.

Strydom, C, Groenewald, E and Potgieter, J (1997) "Thermogravimetric studies of the synthesis of CaS from gypsum, $CaSO_4 \cdot 2H_2O$ and phosphogypsum" *Journal of thermal analysis*, *49*, (3): 1501.

Tao, D, Chen, S, Parekh, BK and Hepworth, MT (2001) "An investigation of a thermochemical process for conversion of gypsum and pyrite wastes into useful products" *Advances in Environmental Research*, *5*, 277–284.

Tesárek, P, Drchalová, J, Kolísko, J, Rovnaníková, P and Černý, R (2007) "Flue gas desulfurization gypsum: Study of basic mechanical, hydric and thermal properties" *Construction and Building Materials*, *21*, (7): 1500–1509.

Thieme, C (2000) "Sodium Carbonates", in: *Ullmann's Encyclopedia of Industrial Chemistry*, Ullmann, F (Ed.), 5th ed. Wiley-VCH, Weinheim.

Tomeczek, J and Palugniok, H (1996) "Specific heat capacity and enthalpy of coal pyrolysis at elevated temperatures" *Fuel*, *75*, (9): 1089–1093.

Tran, H and Barham, D (1981) "The System Na_2SO_4 — Na_2S" in: International Chemical Recovery Conference, Vancouver, Canada, September, 1981.

Trikkel, A and Kuusik, R (1994) "Tallinna tehnikaulik" *Toim. 45*, 742.

Tunsu, C, Petranikova, M, Gergoríc, M, Ekberg, C and Retegan, T (2015) "Reclaiming rare earth elements from end-of-life product: A review of the perspectives for urban mining using hydrometallurgical unit operations" *Hydrometallurgy*, *156*, 239–258.

Ullmann, F, ed. (2008) *Ullmann's Encyclopedia of Industrial Chemistry*, 6th ed. Wiley-VCH, Weinheim.

van Vuuren, D and Maree, J (2018) *A novel process to recover sulfur, lime and rare earths from gypsum* Internal report Department of Chemical Engineering, University of Pretoria.

Van Krevelen, DW (1961) *Coal: Typology, Chemistry, Physics, Constitution*, 2nd ed. Elsvier, Amsterdam.

Walawalkar, M, Nichol, CK and Azimi, G (2016) *Process investigation of the acid leaching of rare earth elements from phosphoogypsum using HCl, HNO_3 and H_2SO_4* URL: `http://dx.doi.org/10.1016/j.hydromet.2016.06.808` (visited on 11/20/2019).

Welty, JR, Wicks, CE and Wilson, RE (1969) *Fundamentals of Momentum, Heat, and Mass Transfer*, 5th ed. Wiley, New York.

White, J and White, A (1936) "Manufacture of sodium sulfide: reduction of sodium sulfate to sodium sulfide at temperatures below 800 °C" *Industrial & Engineering Chemistry*, *28*, (2): 244–246.

Windholz, M (1983) *The Merck Index*, 10th ed. Merck & Co., Inc., New Jersey.

World Trade Organisation (2018a) *South Africa Carbonates; calcium carbonate imports by country in 2018* URL: `https://wits.worldbank.org/trade/comtrade/en/country/ZAF/year/2018/tradeflow/Imports/partner/ALL/product/283650` (visited on 05/10/2021).

World Trade Organisation (2018b) *South Africa Carbonates; disodium carbonate imports by country in 2018* URL: https://wits.worldbank.org/trade/comtrade/en/country/ZAF/year/2018/tradeflow/Imports/partner/ALL/product/283620 (visited on 05/10/2021).

World Trade Organisation (2018c) *South Africa Sulphur; crude or unrefined imports by country in 2018* URL: https://wits.worldbank.org/trade/comtrade/en/country/ZAF/year/2018/tradeflow/Imports/partner/ALL/product/250310 (visited on 05/10/2021).

Xinzheng, B (2020) "Iron oxide reduction reaction tank and preparation method thereof", *CN111359544A*, assigned to Powder Metallurgy Co. LTD, China.

Yan, B, Ma, L, Ma, J, Zi, M and Yan, X (2014) "Mechanism analysis of CaS transformation in phosphogypsum decomposition with Fe catalyst" *Industrial & Engineering Chemistry Research*, *53*, 7648–7654.

Yicheng, F (2014) "Downstream type tunnel kiln for coal-based direct reduced iron and production process therefor", *WO2014169442A1*, assigned to Invest, Dev. Corp. LTD, China.

Yunusova, SS (2004) "Composite Wall Materials and Products Based on Phosphogypsum, Obtained by Semi-Dry Pressing" Dissertation, Samara State Architecture Academy, Samara, Russia.

Zadick, T, Zavaleta, R and McCandless, F (1972) "Catalytic reduction of calcium sulfate to calcium sulfide with carbon monoxide" *Industrial & Engineering Chemistry Research*, *11*, 283.

Zhang, W, Li, X, Qu, Z, Zhao, Q and Chen, G (2010) "Facile solution synthesis and characterization of $CaCO_3$ microspheres with urchin-shaped structure" *Materials Letters*, *64*, 71–73.

Zhang, X, Song, X, Sun, Z, Li, P and Yu, J (2012) "Density functional theory study on the mechanism of calcium sulfate reductive decomposition by carbon monoxide" *Industrial & Engineering Chemistry Research*, *51*, 6563–6570.

Zhongji, H (2012) "Energy-conservation high-efficiency reduction sponge iron tunnel kiln", *CN102643944A*, assigned to Kiln & Furnace Co. LTD, China.

Appendix A Python code for transient modelling

In [51]:

```
#imports
from numpy import linspace, array, interp
from matplotlib import pyplot as plt
import numpy as np
import pandas as pd
from scipy.optimize import fsolve, curve_fit
from matplotlib import rc
from scipy.integrate import solve_ivp
from operator import itemgetter
import matplotlib.gridspec as gridspec
# rc("text", usetex=True)
rc("font", family="serif")
%matplotlib inline
# %matplotlib notebook
```

In [52]:

```
#Coal
#ρB -> https://www.engineeringtoolbox.com/classification-coal-d_164.html
#Cp -> Convection Heat Transfer (4th Edition) + https://www.engineeringtoolbox.com/specific
#k -> Convection Heat Transfer (4th Edition) @ 20degC
#averages of bituminous
ρB_coal = 735 #(673+913)/2 #kg/m3 #735
Cp_coal = 1380 #J/kg.K #1260
k_coal = 0.26 #W/m.K
```

In [53]:

```
#Gypsum
#ρB -> http://www.anval.net/downloads/bulk%20density%20chart.pdf + https://www.binmaster.co
#Cp -> Perry, Convection Heat Transfer (4th Edition) @ 20 degC
#k -> Perry, Convection Heat Transfer (4th Edition) @ 20 degC, Heat Transfer
ρB_gypsum = 721.1 #860 #kg/m3 #721
Cp_gypsum = 1080 # 1090 #J/kg.K
k_gypsum = 0.43 #W/m.K #0.51, 0.48
```

In [54]:

```
#Gypsum+coal mixture at ratio of 1:0.35
#3" SCH 40
h_pot, do_pot = 0.24, 0.0889 #m
di_pot = 0.07792 #m
A_pot = np.pi*(do_pot**2 - di_pot**2)/4 #m2
Ai_pot = np.pi*(di_pot**2)/4
#Bulk density of mixture with above ratio in 3" pot:
M_l = np.array([350.07, 400.05, 500.05]) / 1000 #g -> kg
H_l = (240-np.array([155, 140, 110])) / 1000 #mm -> m
V_l = H_l * Ai_pot #m3
ρ_l = M_l/(V_l) #kg/m3
ρB_mix = np.average(ρ_l)
print("ρB_mix: ", round(ρB_mix,3), "kg/m3")
```

```
ρB_mix:  836.416 kg/m3
```

In [55]:

```
#Molar masses of species
MM_CaSO4 = 136.14
MM_CaS = 72.143
MM_C = 12.0107
MM_CaO = 56.0774
MM_CO = 28.0134
MM_CO2 = 44.01
MM_SO2 = 64.066
```

In [56]:

```
#ρ of reaction species
#Physical Constants of Inorganic Compounds
ρ_CaSO4 = 2.960 #g/cm3
ρ_C = 2.267 #g/cm3
ρ_CaS = 2.59 #g/cm3
ρ_CaO = 3.34 #g/cm3
```

In [57]:

```
#Cp of reaction species
def Cp_CaSO4(T): #Yaws 53
    A, B, C, D, E, F, G = 0.51569101582470012, 0.00072529630914, 0, 0, 0, 0, 0
    Cp = A + B*T + C*T**2 + D*T**3 + E*T**4 + F*T**5 + G*T**6 #kJ/(kg.K)
    Cp = Cp * 1000 # -> J/kg.K
    return Cp

def Cp_CaS_NIST(T):
    t = T/1000
    A, B, C, D, E, F, G, H = 48.60260, 7.280161, -1.933724, 0.329739, -0.289224, -488.9966,
    Cp = A + B*t + C*t**2 + D*t**3 + E/t**2 #J/mol.K
    Cp = Cp * 1000 / MM_CaS #J/mol.K -> J/kg.K
    return Cp

def Cp_CaO_NIST(T):
    t = T/1000
    A, B, C, D, E, F, G, H = 49.95403, 4.887916, -0.352056, 0.046187, -0.825097, -652.9718,
    Cp = A + B*t + C*t**2 + D*t**3 + E/t**2 #J/mol.K
    Cp = Cp * 1000 / MM_CaO #J/mol.K -> J/kg.K
    return Cp

Cpl_C = np.array([0.151961, 0.5172]) * 4.184 * 1000 #cal/g.K -> J/kg.K #Specific heat of in
Tl_C = [273, 1373]

pC = np.polyfit(Tl_C, Cpl_C, 1)
print(pC)

def Cp_C(T):
    a, b = pC
    return a*T+b
```

```
[  1.38923634 256.54330268]
```

Basis: 10 kg coal+gypsum mixture

C charged in 0.5 mol excess =>

$$CaSO_4 + 2.5C \rightarrow CaS + 2CO_2$$

Fixed C in Coal = 34.6 wt % | $CaSO_4$ in Gypsum = 91.41 wt %

Coal fed = 3.682 kg | Gypsum fed = 6.318 kg

Fixed C = 1.274 kg = 0.1061 kmol | $CaSO_4$ = 5.776 kg = 0.0424 kmol

In [58]:

```
#feed calculations
#Gypsum:
df = pd.read_csv("Misc/gypsum_analysis_new.csv")
df["Mole"] = df["Mass %"] / df["MM"]
nT = df["Mole"].sum()
df["Mol %"] = df["Mole"] / nT

#Coal (AD)
X_H2O, X_Ash, X_Vol, X_FixC = 0.027, 0.161, 0.248, 0.564
```

In [59]:

```
x_CaSO4 = df["Mol %"][4]
n_CaSO4 = x_CaSO4 * nT
X_CaSO4 = n_CaSO4 * MM_CaSO4
X_CaSO4
```

Out[59]:

```
0.8982549119609682
```

In [60]:

```
#guess value
Feed = 10 #kg
m_gypsum = 6 #kg

def MB(m_gypsum):
    m_CaSO4 = m_gypsum * X_CaSO4
    n_CaSO4 = m_CaSO4 / MM_CaSO4
    n_FixC = 2.5 * n_CaSO4
    m_FixC = n_FixC * MM_C
    m_coal = m_FixC / X_FixC
    X = m_gypsum + m_coal - Feed
    return X

m_gypsum = fsolve(MB, m_gypsum)[0]
m_coal = Feed - m_gypsum
print("Mass gypsum:",round(m_gypsum,4),"kg")
print("Mass coal:",round(m_coal,4),"kg")
print("Ratio coal to gypsum:", round(m_coal/m_gypsum,4))
```

```
Mass gypsum: 7.4004 kg
Mass coal: 2.5996 kg
Ratio coal to gypsum: 0.3513
```

Kinetic simulation of 1 mol reaction to obtain heat generated term

In [61]:

```
#Reduction kinetics kato et al (2012)
#1 mol CaSO4 fed:
k10, k20 = 3.2e15, 1.6e15 #/mol.s
E1, E2 = 370, 400 #kJ/mol
R = 8.314
n0_CaSO4, n0_C = 1, 2.5
n0_CaS, n0_CaO = 0, 0
hr = 10 #degC/min

def k_T(T):
    k1 = k10*np.exp(-E1*1000/(R*T))
    k2 = k20*np.exp(-E2*1000/(R*T))
    return [k1, k2]

def DEs(t, var):
    n_CaSO4, n_CaS, n_CaO, n_C = var
    T = 298.15 + t * (hr/60)
    if T > 1273.15:
        T = 1273.15
    k1, k2 = k_T(T)
    dn_CaSO4dt = -k1*n_CaSO4*n_C - 3*k2*n_CaSO4*n_CaS
    dn_CaSdt = k1*n_CaSO4*n_C - k2*n_CaSO4*n_CaS
    dn_CaOdt = 4*k2*n_CaSO4*n_CaS
    dn_Cdt = -2*k1*n_CaSO4*n_C
    return [dn_CaSO4dt, dn_CaSdt, dn_CaOdt, dn_Cdt]

t_bound = [0*3600, 2*3600]
init = np.array([n0_CaSO4, n0_CaS, n0_CaO, n0_C])

val_t = solve_ivp(DEs, t_bound, init, dense_output=True)
```

In [62]:

```
#Conc vs t
t_span = linspace(t_bound[0], t_bound[1], 400)
smooth_values = val_t.sol(t_span)
n_CaSO4, n_CaS, n_CaO, n_C = smooth_values

T_span = 25 + t_span * (hr/60)
T_span = [1000 if x > 1000 else x for x in T_span]
```

In [63]:

```
def kinetic_profile(s, X, ylabel):
    ts, Ts = s
    n_CaSO4, n_C, n_CaS, n_CaO = X
    fig, ax1 = plt.subplots()

    ax1.set_xlabel('Time (h)')
    ax1.set_ylabel(ylabel)
    ax1.plot(ts/3600, n_CaSO4, label="CaSO$_4$")
    ax1.plot(ts/3600, n_C, label="C")
    ax1.plot(ts/3600, n_CaS, label="CaS")
    ax1.plot(ts/3600, n_CaO, label="CaO")
    ax1.tick_params(axis='y')

    ax2 = ax1.twinx()  # initialise a second axis that shares the same x-axis

    ax2.set_ylabel('Temperature ($\degree$C)')
    ax2.plot(ts/3600, Ts, "--", color='black', label="Temperature")
    ax2.tick_params(axis='y')

    # ask matplotlib for the plotted objects and their labels
    lines, labels = ax1.get_legend_handles_labels()
    lines2, labels2 = ax2.get_legend_handles_labels()
    ax2.legend(lines + lines2, labels + labels2, loc="best")

    fig.tight_layout()

kinetic_profile([t_span, T_span], [n_CaSO4, n_C, n_CaS, n_CaO], 'Moles (mol)')
# plt.savefig("Figures/Model/kinetic_profile.PNG", dpi=120)
```

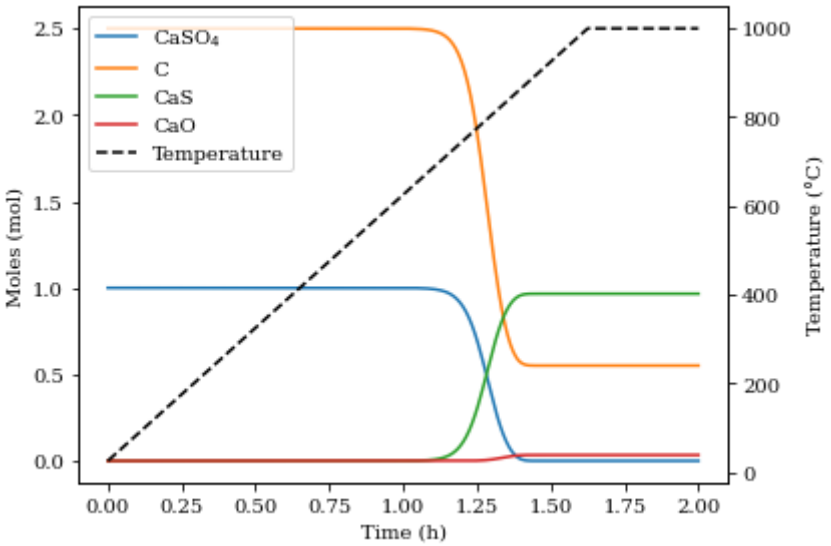

In [64]:

```
def mix_comp(t): #returns mass of species
    CaSO4 = np.interp(t, t_span, C_CaSO4)*MM_CaSO4
    C = np.interp(t, t_span, C_C)*MM_C
    CaS = np.interp(t, t_span, C_CaS)*MM_CaS
    CaO = np.interp(t, t_span, C_CaO)*MM_CaO
    return [CaSO4, C, CaS, CaO]

def mix_prop(X):
    T, t = X
    comp = np.array(mix_comp(t))
    mf = comp/sum(comp)
    mf[mf < 0] = 0

    km = vf0_g*k_gypsum + vf0_c*k_coal
    ρm = ρB_mix
    Cpm = mf[0]*Cp_CaSO4(T) + mf[1]*Cp_C(T) + mf[2]*Cp_CaS_NIST(T) + mf[3]*Cp_CaO_NIST(T)

    return [km, ρm, Cpm]
```

In [65]:

```
#Where the reaction begins
i = np.where(n_CaS > 0.001)[0][0]
rx_Ti = T_span[i]
ti_rx = t_span[i]
print("Reaction start: ", round(ti_rx/3600,2), "h")
print("Reaction start: ", round(T_span[i],2), "degC")

#difference array to use in finding the end of the reaction
diff = [abs(x-y) for x, y in zip(n_CaS[:-1], n_CaS[1:])]
diff = np.array(diff)

#Where the reaction ends
j = np.where(diff[i:] <= 0.000001)[0][0]
print("Reaction end: ", round(t_span[i+j]/3600,2), "h")

rx_tf = t_span[i+j]-t_span[i]
print("Reaction duration: ", round((rx_tf)/3600,2), "h")
```

```
Reaction start:  1.04 h
Reaction start:  650.56 degC
Reaction end:  1.46 h
Reaction duration:  0.42 h
```

In [66]:

```
#Reaction enthalpy - kJ/mol
rx_DF = pd.read_csv("Misc/reaction_enthalpy.csv")

t_rx = rx_DF["t"]
T_rx = rx_DF["T"]
H_rx = rx_DF["deltaH"]
```

In [67]:

```
#Heat generation for 1 mol:
m_g = n0_CaSO4/X_CaSO4*MM_CaSO4 #g
m_c = m_coal/m_gypsum * m_g
m_feed = m_g+m_c #g
V_feed = m_feed/1000 / ρB_mix #m3
print('Volume feed:', round(V_feed*1000,3), 'L')
e_gen = n0_CaSO4*H_rx[39]*1000 / rx_tf / V_feed #mol * J/mol / s / m3 = W / m3
print("Heat generated: ", round(e_gen/1000, 2), "kW/m3")
```

```
Volume feed: 0.245 L
Heat generated:  418.36 kW/m3
```

Simulation of 15 kg original intended

In [68]:

```
#Reduction kinetics kato et al (2012)

#feed:
load = 15 #kg
m_g = m_gypsum/Feed * load
m_c = load - m_g
V_load = load / ρB_mix
n0_CaSO4, n0_C = (m_g*X_CaSO4)/MM_CaSO4*1000, (m_c*X_FixC)/MM_C*1000
n0_CaS, n0_CaO = 0, 0
hr = 10 #degC/min

t_bound = [0*3600, 2*3600]
init = np.array([n0_CaSO4, n0_CaS, n0_CaO, n0_C])

val_t = solve_ivp(DEs, t_bound, init, dense_output=True)
```

In [69]:

```
#Conc vs t
t_span = linspace(t_bound[0], t_bound[1], 400)
smooth_values = val_t.sol(t_span)
n_CaSO4, n_CaS, n_CaO, n_C = smooth_values

T_span = 25 + t_span * (hr/60)
T_span = [1000 if x > 1000 else x for x in T_span]
```

In [70]:

```
kinetic_profile([t_span, T_span], [n_CaSO4, n_C, n_CaS, n_CaO], 'Moles (mol)')
# plt.savefig("Figures/Model/kinetics_15kg.PNG", dpi=120)
```

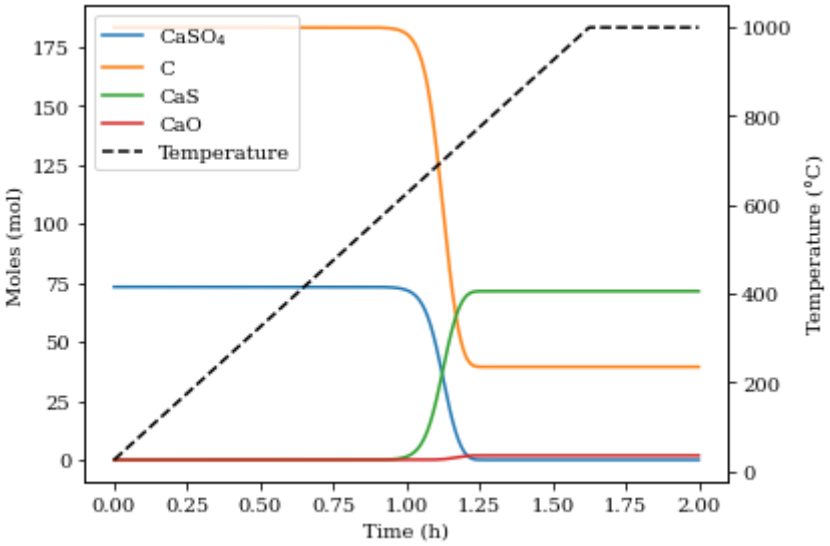

In [71]:

```
km0, km1 = 0.377, 1
Tkm0, Tkm1 = 298.15, 1273.15 #K

pC = np.polyfit([Tkm0, Tkm1], [km0, km1], 1)
print(pC)

def km_fit(T):
    a, b = pC
    return a*T+b
```

```
[0.00063897 0.18648979]
```

In [72]:

```
Ts = np.linspace(Tkm0, Tkm1)
plt.plot(Ts, km_fit(Ts))
plt.plot([Tkm0, Tkm1], [km0, km1], 'o')
```

Out[72]:

```
[<matplotlib.lines.Line2D at 0x1e023a0f4e0>]
```

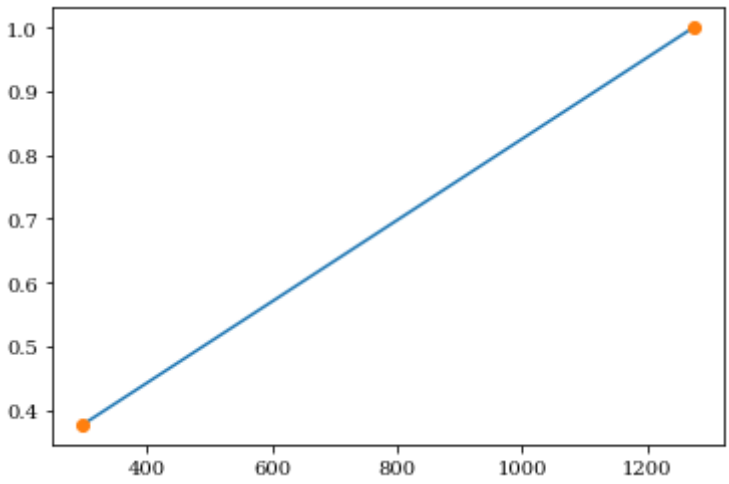

Simulation of multiple configurations

In [73]:

```
def sim(load, di_pot, M, t, sens, heat):
    M_x = M
    Ai_pot = np.pi*(di_pot**2)/4
    h_mix = load / ρB_mix / Ai_pot

    m_g = m_gypsum/Feed * load
    m_c = load - m_g
    n0_CaSO4, n0_C = (m_g*X_CaSO4)/MM_CaSO4*1000, (m_c*X_FixC)/MM_C*1000
    n0_CaS, n0_CaO = 0, 0

    v0_g = m_g/ρB_gypsum
    v0_c = m_c/ρB_coal
    V0 = v0_g+v0_c
    vf0_g, vf0_c = v0_g/V0, v0_c/V0

    km0, km1 = vf0_g*k_gypsum + vf0_c*k_coal, 1
    Tkm0, Tkm1 = 298.15, 1273.15 #K

    pC = np.polyfit([Tkm0, Tkm1], [km0, km1], 1)

    def km_fit(T):
        a, b = pC
        return a*T+b

    def repeated_matrix(initial_matrix): #2D matrix repeated for every time interval
        matrix_list = []
        for i in range(ts):
            matrix_list.append(initial_matrix)
        return np.array(matrix_list)

    def mix_prop(T, X):
        n_CaSO4, n_C, n_CaS, n_CaO = X
        comp = np.array([n_CaSO4*MM_CaSO4, n_C*MM_C, n_CaS*MM_CaS, n_CaO*MM_CaO])/1000 #kg
        mf = comp/sum(comp)
        mf[mf < 0] = 0

        m0 = (n0_CaSO4*MM_CaSO4 + n0_C*MM_C)/1000 / (n_nodes)
        cf = ρB_mix / (m0/(V0/n_nodes))

        km = vf0_g*k_gypsum + vf0_c*k_coal
#         km = km_fit(T)
        ρm = sum(comp)/(V0/n_nodes) * cf
        Cpm = mf[0]*Cp_CaSO4(T) + mf[1]*Cp_C(T) + mf[2]*Cp_CaS_NIST(T) + mf[3]*Cp_CaO_NIST(

        return [km, ρm, Cpm]

    def kinetics(T, var):
        CaSO4, C, CaS, CaO = var
        k1 = k10*np.exp(-E1*1000/(R*T))
        k2 = k20*np.exp(-E2*1000/(R*T))
        CaSO4_i_n = (-k1*CaSO4*C - 3*k2*CaSO4*CaS)*δt + CaSO4
        C_i_n = (-2*k1*CaSO4*C)*δt + C
        CaS_i_n = (k1*CaSO4*C - k2*CaSO4*CaS)*δt + CaS
        CaO_i_n = (4*k2*CaSO4*CaS)*δt + CaO
        if CaSO4_i_n < 0:
            CaSO4_i_n = 0
        return [CaSO4_i_n, C_i_n, CaS_i_n, CaO_i_n]

    #Stability criteria
```

```
    # Δx = Δy = l
    l = (di_pot/2)/(M_x-1)
    M_y = int(round(h_mix/l,0))
    if M_y == 0 or h_mix < 0.2*di_pot or h_mix > 3*di_pot:
#     if M_y == 0:
#         return [[[[273.15]]], 273.15, 0, 0, 0, 0, 0, -4]
        return [[[[273.15]]], 273.15, 0, 0, h_mix, l, [M_x, M_y], 0, 0, 0]
    while M_y < 10:
        M_x += 2
        l = (di_pot/2)/(M_x-1)
        M_y = int(round(h_mix/l,0))
    else:
        n_nodes = M_x*M_y
        nd0_CaSO4 = n0_CaSO4/n_nodes
        nd0_C = n0_C/n_nodes
        nd0_CaS = n0_CaS/n_nodes
        nd0_CaO = n0_CaO/n_nodes
        V_node = load / (M_x*M_y) / ρB_mix #m3

        k_mix, ρ_mix, Cp_mix = mix_prop(Tf, np.array([0, n0_C-n0_CaSO4, n0_CaSO4, 0])/n_noc

        α = k_mix / (ρ_mix * Cp_mix)
        Δt = (l**2)*0.25/(α)
        ts = int((t*3600/Δt)) * 2
        #Transient discretisation, crucible
        δt = t*3600/ts
        τ = α*δt/(l**2)
        τ_max = -5

        Tl = np.arange(Ti, Tf, hr/60*δt)
        Tl2 = np.repeat(Tl[-1], (ts-len(Tl)))
        Tl = np.append(Tl, Tl2)
        tl = linspace(0, t, ts)
        #Calculation
        Cp_test = np.array(())
        ρ_test = np.array(())

        ini_node_matrix = np.zeros((M_y, M_x))
        #2D node temperature matrix set to initial temperature
        ini_node_matrix[ini_node_matrix < 1] = Ti
        #2D mole matrices set to initial moles charged per node
        ini_nCaSO4_m = ini_node_matrix/Ti * nd0_CaSO4
        ini_nC_m = ini_node_matrix/Ti * nd0_C
        ini_nCaS_m = ini_node_matrix/Ti * nd0_CaS
        ini_nCaO_m = ini_node_matrix/Ti * nd0_CaO

        #matrix[time][y-pos][x-pos]
        #3D node temperature matrix through time
        nT_m = repeated_matrix(ini_node_matrix)
        #3D mole matrices through time
        nCaSO4_m = repeated_matrix(ini_nCaSO4_m)
        nC_m = repeated_matrix(ini_nC_m)
        nCaS_m = repeated_matrix(ini_nCaS_m)
        nCaO_m = repeated_matrix(ini_nCaO_m)

        for i, Tval in enumerate(Tl):
            if i>0:
                r = di_pot/2 #this should be from the outside r=r to centre r=0
                #previous time step, current time step
                T_i, T_i_n = nT_m[i-1], nT_m[i]
                CaSO4_i, CaSO4_i_n = nCaSO4_m[i-1], nCaSO4_m[i]
```

```
                C_i, C_i_n = nC_m[i-1], nC_m[i]
                CaS_i, CaS_i_n = nCaS_m[i-1], nCaS_m[i]
                CaO_i, CaO_i_n = nCaO_m[i-1], nCaO_m[i]

                for jx in range(M_x): #ramping exterior x & y values according to heating r
                    T_i_n[0][jx] = Tval
                for jy in range(M_y):
                    T_i_n[jy][0] = Tval

                k_mix, ρ_mix, Cp_mix = mix_prop(T_i[0][0], [nCaSO4_m[i-1][0][0], nC_m[i-1][
                Cp_test = np.append(Cp_test, Cp_mix)
                ρ_test = np.append(ρ_test, ρ_mix)

                if sens == True and T_i[-1][-1] >= 950+273.15:
                    nTf_l = np.array(list(map(itemgetter(-1), (list(map(itemgetter(-1), nT_
                    return[nT_m, T_i[-1][-1], δt, i+1, h_mix, l, [M_x, M_y], τ_max, Cp_test

                for jx in range(M_x): #calculating new temperature per y slice
                    for jy in range(M_y): #does whole column of y then moves onto next x
                        #Calculation of kinetics
                        CaSO4_i_n[jy][jx], C_i_n[jy][jx], CaS_i_n[jy][jx], CaO_i_n[jy][jx]
                        #Heat of reaction
                        δn = abs(CaSO4_i_n[jy][jx] - CaSO4_i[jy][jx])
                        if heat == True:
                            e_g = δn*(H_rx[39]*1000) / δt / V_node #mol * J/mol / s / m3 =
                        else:
                            e_g = 0

                        #calculation of new τ for every node
                        k_mix, ρ_mix, Cp_mix = mix_prop(T_i[jy][jx], [CaSO4_i[jy][jx], C_i[
                        α = k_mix / (ρ_mix * Cp_mix)
                        τ = α*δt/(l**2)

                        if τ > τ_max:
                            τ_max = τ

                        if jy >= 1 and jx >= 1:
                            if jy >= M_y-1 and jx>= M_x-1: #Corner boundary, set m+1=m-1 &
                                T_i_n[jy][jx] = τ*(2*T_i[jy][jx-1]+T_i[jy-1][jx]+2*T_i[jy][
#                                 Cp_test = np.append(Cp_test, Cp_mix)
                            elif jy >= M_y-1: #Bottom boundary, set n+1=n-1
                                T_i_n[jy][jx] = τ*(T_i[jy][jx-1]+T_i[jy-1][jx]+T_i[jy][jx+1
                            elif jx >= M_x-1: #side boundary, set m+1=m-1
                                T_i_n[jy][jx] = τ*(2*T_i[jy][jx-1]+T_i[jy+1][jx]+2*T_i[jy][
                            else:
                                T_i_n[jy][jx] = τ*(T_i[jy][jx-1]+T_i[jy+1][jx]+T_i[jy][jx+1
                    r -= l

#         nTf_l = np.array(list(map(itemgetter(-1), (list(map(itemgetter(-1), nT_m[:i])))))
        return [nT_m, T_i[-1][-1], δt, i+1, h_mix, l, [M_x, M_y], τ_max, [Cp_test, ρ_test],
```

Simulation of 15 kg to generate heat-map

In [74]:

```
Ti, Tf = 25+273.15, 1000+273.15 #K
hr = 10
t = 12
M = 10

load = 15 #kg
h_pot, do_pot = 0.3, 0.3 #m
di_pot = do_pot-0.01

nT_m, Tf_c, δt, i, h_m, l, Mn, τ, props, k_m, moles = sim(load, di_pot, M, t, False, True)
```

In [75]:

```
#Reduction kinetics kato et al (2012)

#feed:
load = 15 / (Mn[0]*Mn[1]) #kg
m_g = m_gypsum/Feed * load
m_c = load - m_g
V_load = load / ρB_mix
n0_CaSO4, n0_C = (m_g*X_CaSO4)/MM_CaSO4*1000, (m_c*X_FixC)/MM_C*1000
n0_CaS, n0_CaO = 0, 0
hr = 10 #degC/min

t_bound = [0*3600, 2*3600]
init = np.array([n0_CaSO4, n0_CaS, n0_CaO, n0_C])

val_t = solve_ivp(DEs, t_bound, init, dense_output=True)

#Conc vs t
t_span = linspace(t_bound[0], t_bound[1], 400)
smooth_values = val_t.sol(t_span)
n_CaSO4, n_CaS, n_CaO, n_C = smooth_values

T_span = 25 + t_span * (hr/60)
T_span = [1000 if x > 1000 else x for x in T_span]

kinetic_profile([t_span, T_span], [n_CaSO4, n_C, n_CaS, n_CaO], 'Moles (mol)')
# plt.savefig("Figures/Model/kinetics_15kg.PNG", dpi=120)
```

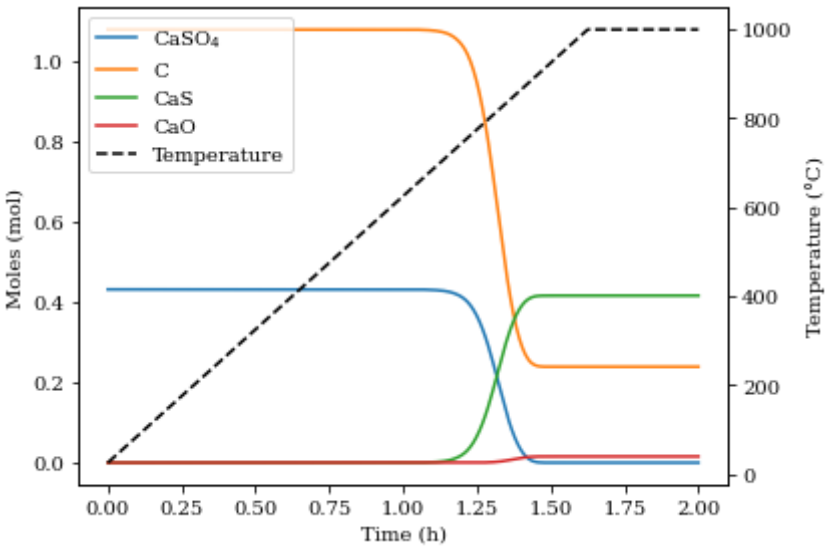

In [76]:

```
ts = int(t*3600/δt)
Tl = np.arange(Ti, Tf, hr/60*δt)
Tl2 = np.repeat(Tl[-1], (ts-len(Tl)))
Tl = np.append(Tl, Tl2)
tl = linspace(0, t, ts)
```

In [77]:

```
CaSO4, C, CaS, CaO = [], [], [], []

for j in range(i-1):
    CaSO4.append(sum(sum(moles[0][j])))
    C.append(sum(sum(moles[1][j])))
    CaS.append(sum(sum(moles[2][j])))
    CaO.append(sum(sum(moles[3][j])))

plt.plot(tl, CaSO4, label="CaSO$_4$")
plt.plot(tl, C, label="C")
plt.plot(tl, CaS, label="CaS")
plt.plot(tl, CaO, label="CaO")
plt.xlabel('Time (h)')
plt.ylabel('Moles (mol)')
plt.legend(loc="best")
# plt.savefig("Figures/Model/kinetics_15kg_full.PNG", dpi=120)
```

Out[77]:

```
<matplotlib.legend.Legend at 0x1e000d00128>
```

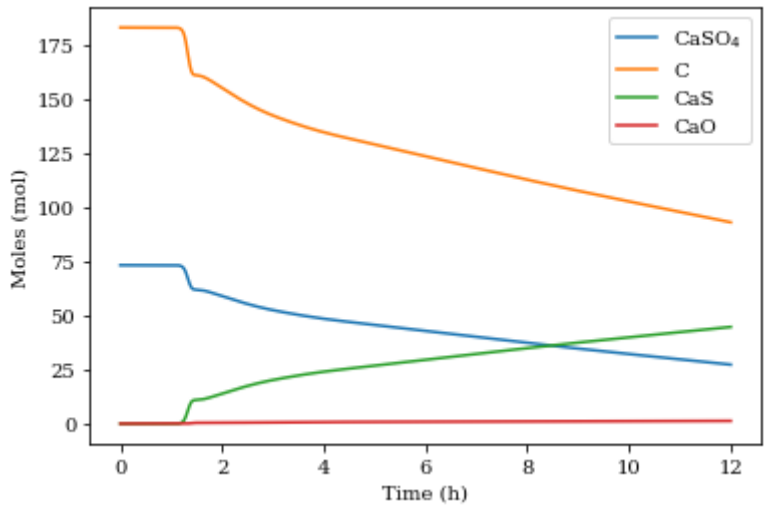

In [78]:

```
T_s = Tl[0:ts]-273.15
t_s = tl[0:ts]
# t_s = linspace(0, t, len(Tl[0:ts-1]))
Cp_l, ρ_l = props[0], props[1]
α_test = k_m/(ρ_l*Cp_l)
τ_test = α_test*δt/(l**2)

def plot_comp(ax, x, label):
    ax.plot(T_s, x)
    ax.set_xlabel('Temperature ($\degree$C)')
    ax.set_ylabel(label)

fig, axs = plt.subplots(2, 2, figsize=(10, 6))
ax1 = axs[0,0]
ax2 = axs[0,1]
ax3 = axs[1,0]
ax4 = axs[1,1]
#         fig.suptitle(file)

ax1.set_title('(a)', y=-0.4)
ax2.set_title('(b)', y=-0.4)
ax3.set_title('(c)', y=-0.4)
ax4.set_title('(d)', y=-0.4)

plot_comp(ax1, Cp_l, 'C$_p$ (J kg$^{-1}$ K$^{-1}$)')
plot_comp(ax2, ρ_l, 'ρ$_B$ (kg m$^{-3}$)')
plot_comp(ax3, α_test, 'α (m$^2$ s$^{-1}$)')
plot_comp(ax4, τ_test, 'τ (-)')

fig.tight_layout()
print(max(τ_test))
# fig.savefig('Figures/Model/prop_mix.png', dpi=120)
```

```
0.12605511127448993
```